

## Neutron-deuteron breakup experiment at $E_n = 13$ MeV: Determination of the $^1S_0$ neutron-neutron scattering length $a_{nn}$

D. E. Gonzalez Trotter,<sup>\*</sup> F. Salinas Meneses,<sup>†</sup> W. Tornow,<sup>‡</sup> C. R. Howell,  
Q. Chen,<sup>§</sup> A. S. Crowell, C. D. Roper,<sup>||</sup> and R. L. Walter

*Department of Physics, Duke University and Triangle Universities Nuclear Laboratory, Durham, NC 27708, USA*

D. Schmidt

*Physikalisch-Technische Bundesanstalt, D-38116, Braunschweig, Germany*

H. Witała

*Institute of Physics, Jagiellonian University, PL-30059 Cracow, Poland*

W. Glöckle

*Institut für Theoretische Physik 2, Ruhr-Universität Bochum, D-44780 Bochum, Germany*

H. Tang and Z. Zhou

*Chinese Institute of Atomic Energy, Beijing, People's Republic of China*

I. Šlaus

*Rudjer Boskovic Institute, Zagreb, Croatia*

(Received 26 April 2005; published 13 March 2006)

We report on results of a kinematically complete neutron-deuteron breakup experiment performed at Triangle Universities Nuclear Laboratory using an  $E_n = 13$  MeV incident neutron beam. The  $^1S_0$  neutron-neutron scattering length  $a_{nn}$  has been determined for four production angles of the neutron-neutron final-state interaction configuration. The absolute cross-section data were analyzed with rigorous three-nucleon calculations. Our average value of  $a_{nn} = -18.7 \pm 0.7$  fm is in excellent agreement with  $a_{nn} = -18.6 \pm 0.4$  fm obtained from capture experiments of negative pions on deuterons. We also performed a shape analysis of the final-state interaction cross-section enhancements by allowing the normalization of the data to float. From these relative data, we obtained an average value of  $a_{nn} = -18.8 \pm 0.5$  fm, in agreement with the result obtained from the absolute cross-section measurements. Our result deviates from the world average of  $a_{nn} = -16.7 \pm 0.5$  fm determined from previous kinematically complete neutron-deuteron breakup experiments, including the most recent one carried out at Bonn. However, this low value for  $a_{nn}$  is at variance with theoretical expectation and other experimental information about the sign of charge-symmetry breaking of the nucleon-nucleon interaction. In agreement with theoretical predictions, no evidence was found of significant three-nucleon force effects on the neutron-neutron final-state interaction cross sections.

DOI: [10.1103/PhysRevC.73.034001](https://doi.org/10.1103/PhysRevC.73.034001)

PACS number(s): 21.45.+v, 25.10.+s, 13.75.Cs

### I. INTRODUCTION

The principle of charge symmetry, i.e., the conjecture that the neutron-neutron ( $nn$ ) and proton-proton ( $pp$ ) nuclear interactions are identical, was proposed in 1932 by Heisenberg [1]. We now know that this symmetry is only approximate. In the spirit of quantum chromodynamics, charge-symmetry breaking (CSB) originates from the mass difference between up and down quarks and electromagnetic energy differences caused

by their different electric charges and magnetic moments [2]. In the meson-exchange picture of the nucleon-nucleon ( $nn$ ) interaction, CSB has its origin in the neutron-proton ( $np$ ) mass difference and in electromagnetic interactions, such as mixing of neutral mesons and irreducible meson-photon exchanges [3]. Spectra of mirror nuclei, especially  $^3\text{H}$  and  $^3\text{He}$  [4], show larger binding energies for the more neutron-rich species, suggesting that the  $nn$  interaction is stronger than the  $pp$  interaction.

The  $^1S_0$  scattering length is directly related to the strength of the  $NN$  interaction, and it is very sensitive to small variations of the nuclear potential. A  $\sim 1\%$  change in the nuclear potential leads to a  $\sim 30\%$  modification of the value for the scattering length, making it an ideal tool for determining the magnitude of CSB [5]. This was the motivation for the early attempts to obtain information on the magnitude of the  $pp$  scattering length  $a_{pp}$  and the  $nn$  scattering length  $a_{nn}$ . Free  $pp$  scattering

<sup>\*</sup>Present address: General Electric Global Research Center, Niskayuna, NY.

<sup>†</sup>Present address: MCI, Clinton, MS.

<sup>‡</sup>Electronic address: tornow@tunl.duke.edu

<sup>§</sup>Present address: MCI, Ashburn, VA.

<sup>||</sup>Present address: Bettis Atomic Power Laboratory, West Mifflin, PA.

experiments resulted in  $a_{pp} = -7.813 \pm 0.004$  fm [6]. For the nuclear ( $N$ )  $^1S_0$   $pp$  scattering length, one obtains from these experiments  $a_{pp}^N = -17.3 \pm 0.3$  fm [2,7], where most of the uncertainty is associated with the model-dependent subtraction of the electromagnetic part of the  $pp$  interaction. The experimental determination of  $a_{nn}$  is considerably more difficult because of the lack of a sufficiently dense free neutron target. First attempts to obtain information on  $a_{nn}$  came from kinematically incomplete neutron-deuteron ( $nd$ ) breakup experiments, where the energy spectrum of the outgoing protons was measured near  $0^\circ$ . These experiments yielded a wide range of values for  $a_{nn}$  (between  $-14.09$  and  $-22.08$  fm), suggesting difficulties in accounting for instrumental effects and/or in properly evaluating the uncertainties associated with the use of simplified  $NN$  potential models and approximate theoretical methods used in the analyses. For a review of kinematically incomplete measurements, we refer to Ref. [8].

Further attempts to obtain more accurate values for  $a_{nn}$  concentrated on kinematically complete  $nd$  breakup experiments [9–12] and on the negative pion-deuteron ( $\pi^-d$ ) capture reaction [13–15] with three and two nucleons, respectively, in the final state. In the first type of experiment, two outgoing neutrons with zero or small relative momentum are detected and the cross section in such a final-state interaction (FSI) configuration is measured. The cross section shows a characteristic enhancement around zero relative momentum of the two neutrons. This enhancement is due to the associated strong  $nn$  interaction in the  $^1S_0$  state, and its sensitivity to the magnitude of  $a_{nn}$  is a powerful method for obtaining experimental information on  $a_{nn}$ . The  $\pi^-d$  experiments determine  $a_{nn}$  from the shape of either the  $\gamma$ -ray energy spectrum alone or the neutron time-of-flight spectrum measured in coincidence with the  $\gamma$  rays.

The average value for  $a_{nn}$  determined from the  $nd$  breakup reaction is  $-16.7 \pm 0.5$  fm [16], while the average value obtained from the  $\pi^-d$  capture reaction is  $-18.6 \pm 0.4$  fm [15]. In Ref. [16] it was suggested that this difference reflects the action of a three-nucleon force (3NF) between the three nucleons involved in the  $nd$  breakup reaction.

The values given above for  $a_{nn}$  are not corrected for the magnetic interaction. The  $nn$  magnetic interaction is repulsive, making the measured value for  $a_{nn}$  more positive by about 0.3 fm [2,7] than the pure nuclear  $^1S_0$  scattering length  $a_{nn}^N$ . The incomplete knowledge of the wave function at short distances contributes an estimated uncertainty of 0.3 fm to the determination of  $a_{nn}^N$ .

During the last 15 years, it has become feasible to solve rigorously the three-nucleon ( $3N$ ) Faddeev equations using modern  $NN$  interactions, and more recently including 3NFs as well [17–19]. With these new powerful theoretical methods at hand, it is now possible to perform experiment-specific theoretical analyses of  $nd$  breakup data which take into account all the details of the experimental setup and simultaneously incorporate state-of-the-art  $3N$  dynamics.

Theoretical sensitivity studies [20] have shown that for  $E_n = 13.0$  MeV, the  $nn$  FSI cross section is practically independent of the particular choice of the  $NN$  interaction used in the  $3N$  calculations if the same value for  $a_{nn}$  is used. Furthermore, the influence of present day  $3N$  models [21–24] vanishes

for a specific production angle region of the  $nn$  pair, while it enhances (lowers) the calculated cross section by only a few percent at smaller (larger) angles [20]. With this observation in mind, we concentrated our experimental effort on the  $nn$  pair production angular range between  $\theta_{nn} = 20^\circ$  and  $43^\circ$  to find out whether our result for  $a_{nn}$  is in any way affected by 3NF effects. Although these effects are predicted to be very small, our strategy should enable us to set at least a limit on the importance of 3NFs on the  $nn$  FSI cross sections.

In this paper, we report absolute cross-section data of four  $nn$  FSI configurations for the kinematically complete  $nd$  breakup reaction induced by 13 MeV neutrons. In Sec. II, details of the experimental setup are given and the determination of the luminosity required for obtaining absolute cross-section data is described. A brief description of the theoretical formalism and the cross-section calculations follows in Sec. III. These theoretical cross sections form the basis for an accurate Monte Carlo simulation, which is presented in Sec. IV. There we discuss also the cross-section results and their uncertainties. In Sec. V, the determination of  $a_{nn}$  from both the absolute cross-section data and the shape of the  $nn$  FSI peaks is described and results for  $a_{nn}$  are given. Finally, we conclude and summarize in Sec. VI.

The results presented for  $a_{nn}$  in this paper were obtained in an experiment that simultaneously measured  $a_{nn}$  and the  $np$  scattering length  $a_{np}$ . The experiment consisted of seven runs, each lasting about 10 days, resulting in a total of 2200h of net data-acquisition time. Our work on the determination of  $a_{np}$  will be described in Part II of this work (Salinas Meneses *et al.* [25]). A short account of our simultaneous determination of  $a_{nn}$  and  $a_{np}$  was given in Ref. [26].

## II. EXPERIMENT

### A. Overview of experimental setup

The neutron beam was produced at the Triangle Universities Nuclear Laboratory (TUNL) using the  $^2\text{H}(d, n)^3\text{He}$  reaction which has a very forward peaked cross section, providing an intense flux of nearly monoenergetic neutrons around  $0^\circ$ . A gas cell filled to 7.8 atm with deuterium was bombarded with an  $E_d = 10.4$  MeV deuteron beam of average current of  $1.8 \mu\text{A}$ . The gas cell consisted of a thin-walled copper cylinder,  $3.0 \times 1.0$  cm in inner length and diameter, with a  $6.35 \mu\text{m}$  thick Havar entrance foil and a gold beam stop of  $0.051$  cm thickness (see Fig. 1). In order to carry away the power deposited in the gas cell by the incident deuteron beam ( $\sim 20$  W), the gas cell was cooled with deionized water and compressed air. The neutron beam was collimated through a double truncated collimator inserted in a shielding wall (see Fig. 2). The collimator is made of tungsten, copper, and polyethylene, resulting in a homogeneous flux of neutrons of mean energy  $E_n = 13.0$  MeV with a total energy spread of  $0.4$  MeV. This beam of rectangular profile was incident on a cylindrical NE-232 deuterated scintillator center detector (CD) located 170 cm from the gas cell. The CD's active volume measured  $6.0 \times 4.0$  cm in height and diameter and was contained in a glass vessel of  $0.22$  cm wall thickness. The glass vessel is attached to a 2 in. photomultiplier tube

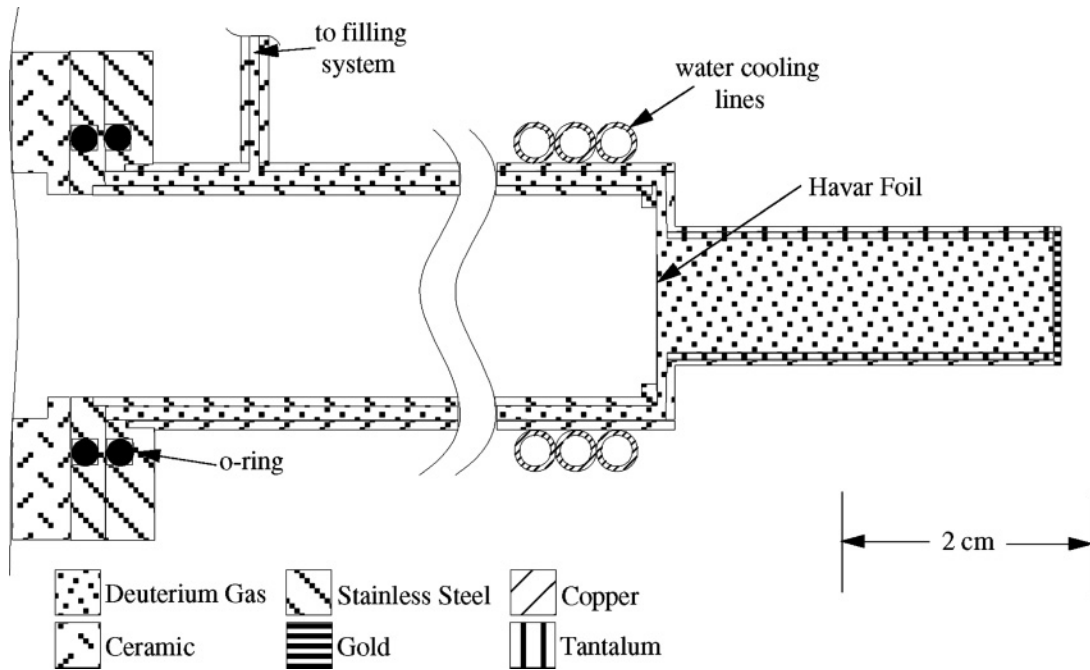


FIG. 1. Lateral cross-section view of gas cell used for the  $^2\text{H}(d,n)^3\text{He}$  reaction.

(PMT). The shielding wall separates the neutron production gas cell from the array of neutron detectors and reduces their count rate from neutrons produced in the gas cell at angles other than  $\sim 0^\circ$ . The multilayered shielding wall is composed of tungsten, copper, iron, steel, lead, paraffin, and concrete.

A total of 16 neutron detectors were placed at 150 cm (ring type and transmission type) and 250 cm (Bicron type) from the CD, with ring-Bicron detector pairs positioned at the  $mn$  FSI laboratory angles of  $\theta_{mn} = 20.5^\circ, 28.0^\circ, 35.5^\circ,$  and  $43.0^\circ$  on the right side of the incident neutron beam, and

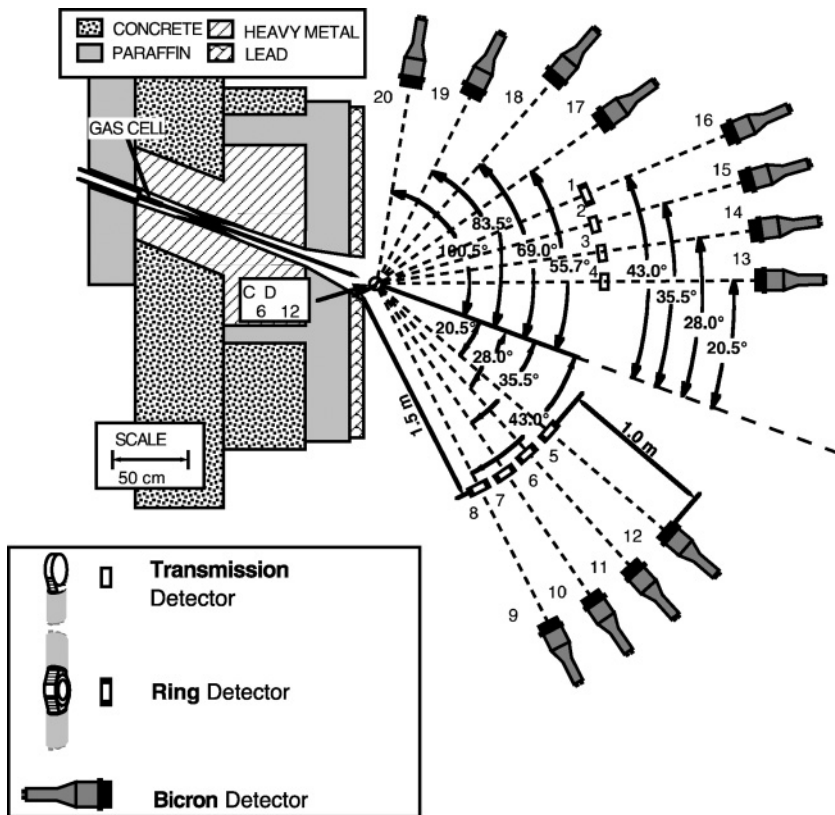


FIG. 2. Layout of detectors for  $a_{mn}$  experiment in the TUNL shielded neutron source experimental area.

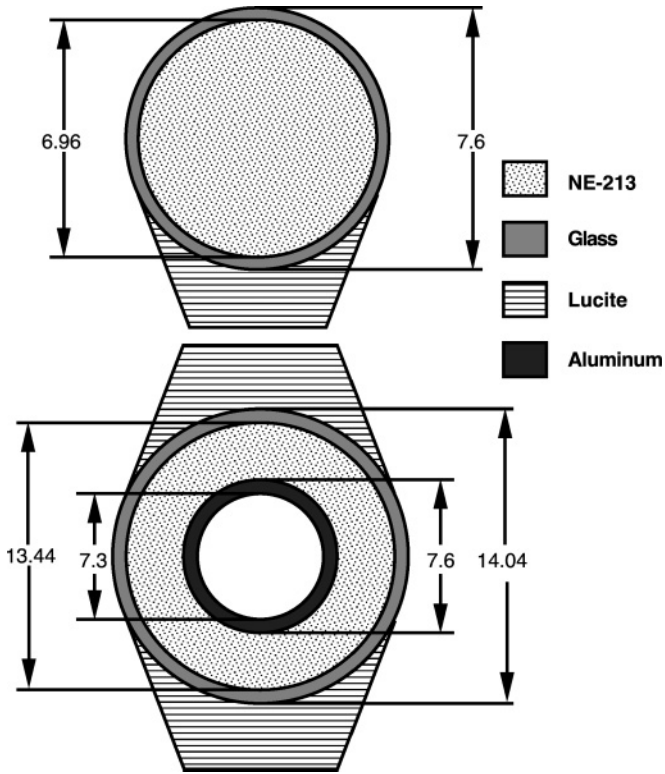


FIG. 3. Front view of ring (bottom of figure) and transmission detectors (top of figure) with light guides (all dimensions in cm).

transmission-Bicron pairs at  $\theta_{nn} = 20.5^\circ, 28.0^\circ,$  and  $35.5^\circ$  and one additional ring-Bicron pair at  $43.0^\circ$  on the left side of the incident neutron beam (see Fig. 2).

A ring detector (see Figs. 3 and 4) consists of a vessel built of two concentric 4 cm high cylindrical walls. The inner wall is made of 1.5 mm thick aluminum. The outer wall is made of 3.2 mm thick glass. Front and back aluminum plates of 1 mm thickness close the space between the concentric walls to complete the vessel. The inner diameter of the scintillator is 7.6 cm, and the outer diameter is 13.44 cm. A small filling pipe and a Teflon tube used as an expansion volume are attached to the front and back plates, respectively. The inside of the vessel is coated with BC-624 reflector paint, except for two windows to allow scintillation light to be transmitted through Lucite light guides to 2 in. PMTs attached to the top and bottom of the ring detector assembly.

The transmission detectors are similar to the ring detectors, except that the liquid scintillator vessel is built out of only one cylindrical glass wall with front and back aluminum plates glued to it. A single window allows scintillation light to escape through a light guide to a PMT. The ring and transmission detector's active volumes consist of NE-213 liquid scintillator.

The Bicron detector vessel is a simple aluminum cylinder, one end of which is a glass window and the opposite end is a 1 mm thick aluminum plate. The inner radius is 6.34 cm and the interior depth is 5.08 cm. The interior surfaces are coated with BC-622 reflector paint. The vessels are mounted directly on a 5 in. PMT. The Bicron detectors are filled with BC-501 liquid scintillator fluid. Teflon tubing wound around the outer cylindrical surface serves as expansion volume.

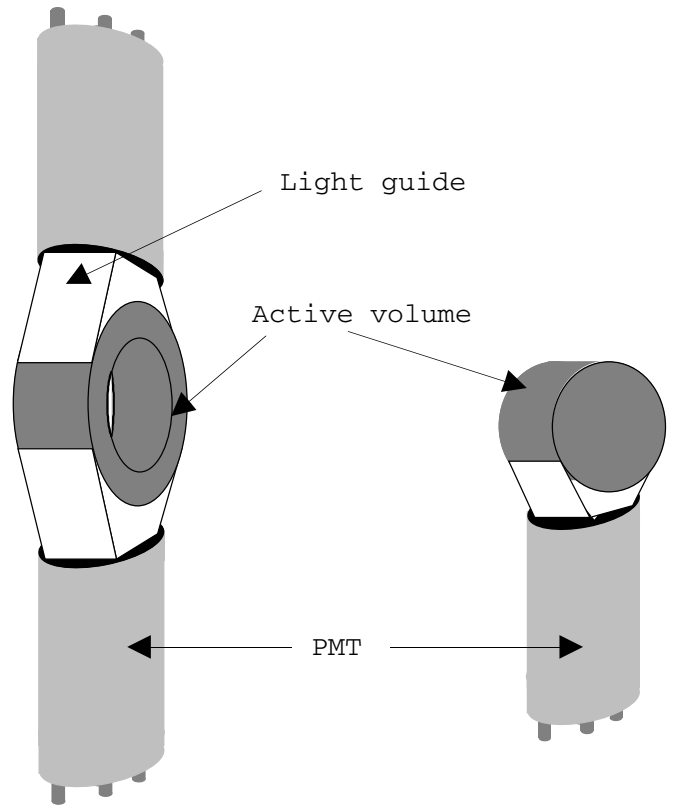


FIG. 4. Sketch of complete ring and transmission detectors.

All detectors were mounted on low-mass holders and placed on stands bolted to the floor. The detectors were accurately positioned at their nominal angles and their nominal height (1.77 m from the floor) using telescopes and laser beams. In the ring-Bicron pair configurations, the ring detector's opening subtends the same solid angle as the active volume of the Bicron detector behind it. The intention is that one neutron from an  $a_{nn}$  FSI event is detected in the ring detector, while the companion neutron travels through the ring's opening and is detected by the Bicron detector. In the transmission-Bicron pair configuration, the transmission detector is placed in front of the Bicron detector, with both active volumes subtending approximately the same solid angle. To register an  $a_{nn}$  FSI event, one neutron must be detected by the transmission detector while the companion neutron passes through it without interaction and is subsequently detected by the Bicron detector.

The four neutron detectors shown on the left side of the incident neutron beam in the angular range from  $55.7^\circ$  to  $100.5^\circ$  were used together with the  $a_{nn}$  detectors positioned on the right side of the incident neutron beam between  $28.0^\circ$  and  $43.0^\circ$  for the simultaneous determination of the  $np$  scattering length  $a_{np}$  (see Ref. [25]).

Both types of detectors (ring and transmission) were constructed because we had no previous experience with ring detectors. Therefore, the transmission detectors served as a backup. However, it turned out that our homemade ring detectors were very stable during the course of the 2yr long experiment. As expected, the ring detectors proved to be far

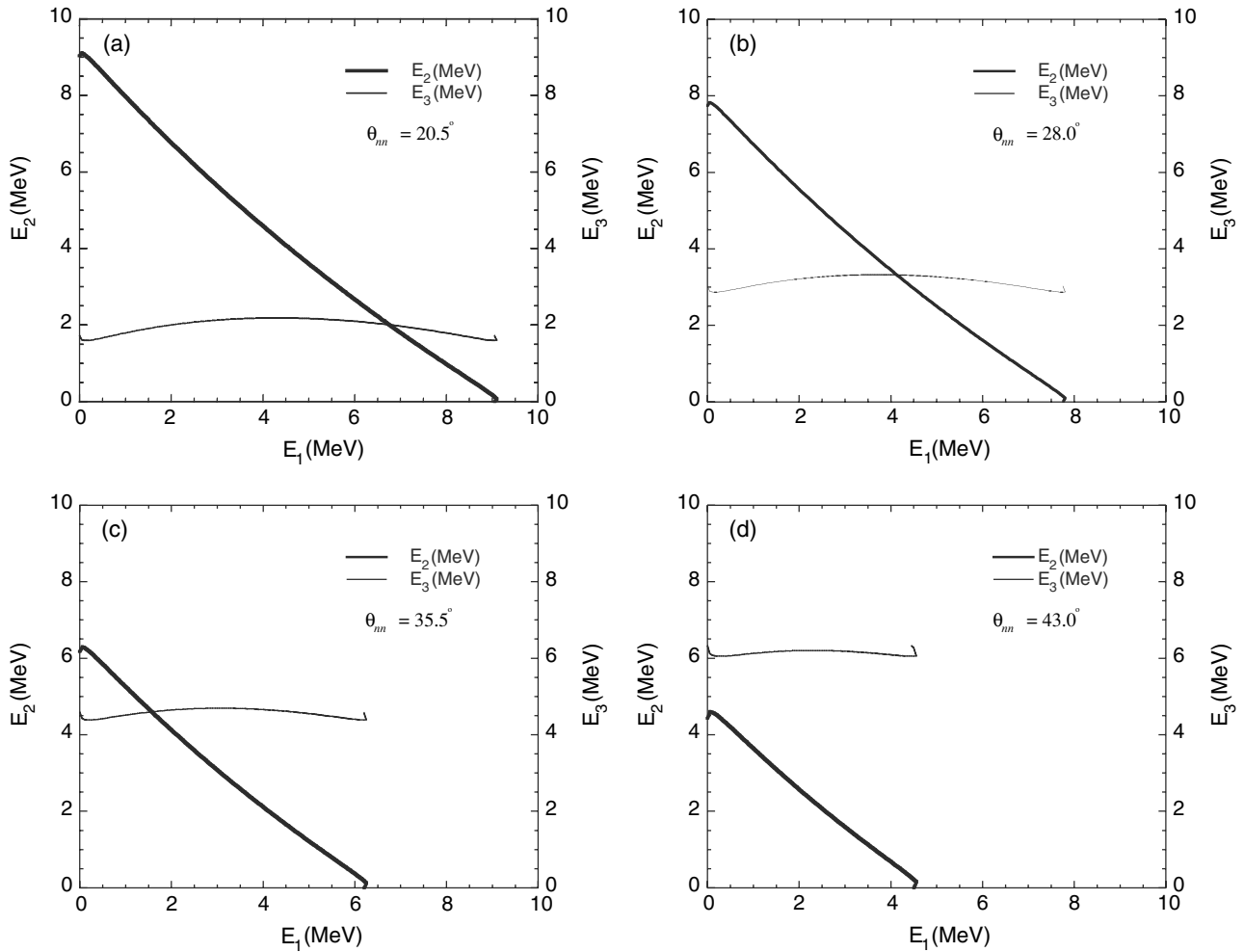


FIG. 5. Kinematic curves for neutron energy  $E_2$  and proton energy  $E_3$  as a function of neutron energy  $E_1$ . Thick curves show the locus of interest for the determination of  $a_{nn}$  at four laboratory angles  $\theta_{nn}$ .

more efficient in the detection of the  $a_{nn}$  events of interest than the transmission detectors. This is because of the larger solid angle subtended by the ring detectors and because the ring detectors do not attenuate the neutron flux intended for detection by the Bicron detectors positioned behind them.

For a given  $nn$  FSI configuration of the  $nd$  breakup reaction  $n + d \rightarrow n_1 + n_2 + p_3$ , the neutron energies  $E_1$  and  $E_2$  as well as the proton energy  $E_3$  were measured. Figures 5(a) through 5(d) show the kinematic loci (thick solid curves) of neutron energy  $E_1$  versus neutron energy  $E_2$  for the four  $nn$  FSI configurations studied in the present work. The thin solid curves give the associated proton energies  $E_3$ .

### B. Detector electronics and data acquisition

The neutron energies  $E_1$  and  $E_2$  were measured using the time-of-flight (TOF) technique. The proton energy  $E_3$  was determined from the pulse-height (PH) signal in the CD. Pulse-shape discrimination (PSD) was applied to the neutron detectors, resulting in an efficient rejection of most of the  $\gamma$ -ray induced events in the neutron detectors. The events of interest were divided into double and triple events. Double

events consisted of the correlated “firing” of the CD and any neutron detector. These events were mostly due to elastic  $nd$  scattering. Triple events consisted of the correlated firing of the CD and any pair of neutron detectors belonging to an  $nn$  FSI configuration. The following is a short description of the electronics and data-acquisition system.

#### 1. Neutron detector electronics

The neutron detector’s anode signals were used to (a) provide a stop signal for the TOF measurements, (b) apply PSD between neutrons and gamma rays, (c) set a hardware lower-level detection threshold, and (d) contribute to the logical signal for the computer trigger circuit.

The hardware threshold was set below the software threshold of  $1/3$  the PH for the  $\gamma$ -ray Compton edge of  $^{137}\text{Cs}$  ( $1/3 \times \text{Cs}$ ). This corresponds to a proton recoil energy threshold of approximately 0.8 MeV. The ring detectors have two PMTs whose anode signals were summed passively. The neutron detector’s dynode signals were integrated by Ortec 113 or by TUNL-made preamplifiers. The two dynode signals from a ring detector were summed before integration. The resulting

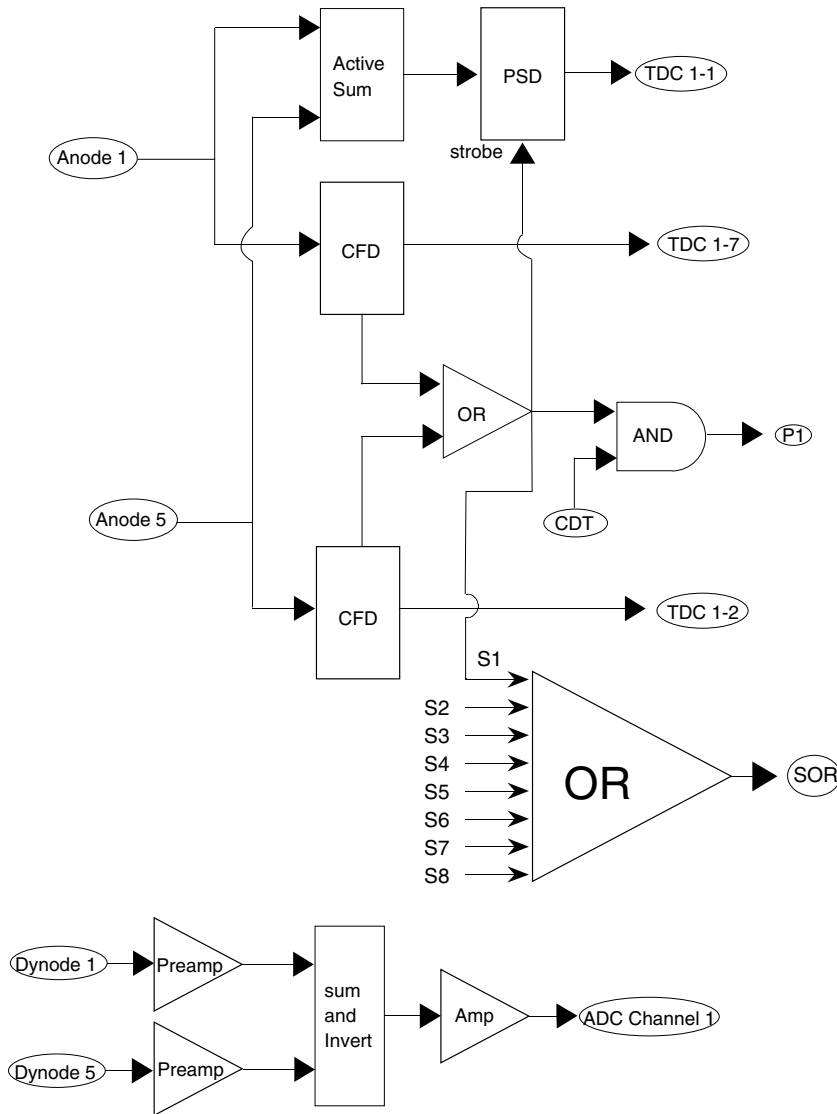


FIG. 6. Simplified electronics diagram for neutron detector electronic pair 1.

signal was amplified and sent to an analog-to-digital (ADC) converter. The neutron detector electronics were grouped in pairs because of limited availability of electronic modules and ADC channels. Figure 6 shows the detection electronics associated with detector pair 1, consisting of detectors 1 and 5 (see Fig. 2 for labeling). The constant-fraction-discriminator (CFD) signal of each detector of an electronic pair is directed into a logical OR, whose output in coincidence with a CD logical signal (see Fig. 7) provides an input to the computer trigger circuit. Some of the neutron detectors were equipped with light-emitting diodes (LEDs) to measure the dead time of the entire data-acquisition system (see Sec. II B 3). The gain stability of each individual neutron detector was monitored every 12 h by determining the Compton edge of its  $^{137}\text{Cs}$  pulse-height spectrum.

### 2. Center detector electronics

The CD anode signal provides timing information from *nd* breakup and *nd* elastic scattering events in this deuterated liquid scintillator target. The CD anode signal is taken into a CFD which also determines the PH threshold. A threshold of

$1/11 \times \text{Cs}$  was used for the CD, corresponding to a deuteron recoil energy (from elastic *nd* scattering) of approximately 300 keV or a proton energy (from *nd* breakup) of approximately 200 keV. For the energy signals, the two dynode outputs 10 (low gain) and 11 (high gain) of the 14-stage PMT were used to cover the full dynamic range of pulse heights of interest. These dynode pulses were independently amplified and then selected at linear gate modules by the coincidence output from the computer trigger (see Fig. 8). This reduces the rate of CD linear signals from  $\sim 400$  kHz down to  $\sim 100$  Hz. Finally, the gated low- and high-gain pulses go to main amplifiers whose outputs are digitized by ADCs. The CD was equipped with two LEDs for electronic dead-time measurements (see Sec. II B 3). The stability of the CD gain was monitored every 12 h by determining the PH of the Compton edge of a  $^{137}\text{Cs}$   $\gamma$ -ray source.

### 3. Computer trigger electronics

The computer trigger circuit provides common start signals and gates for the time-to-digital converters (TDCs) and ADCs. The trigger's coincidence output is used by fast linear gate

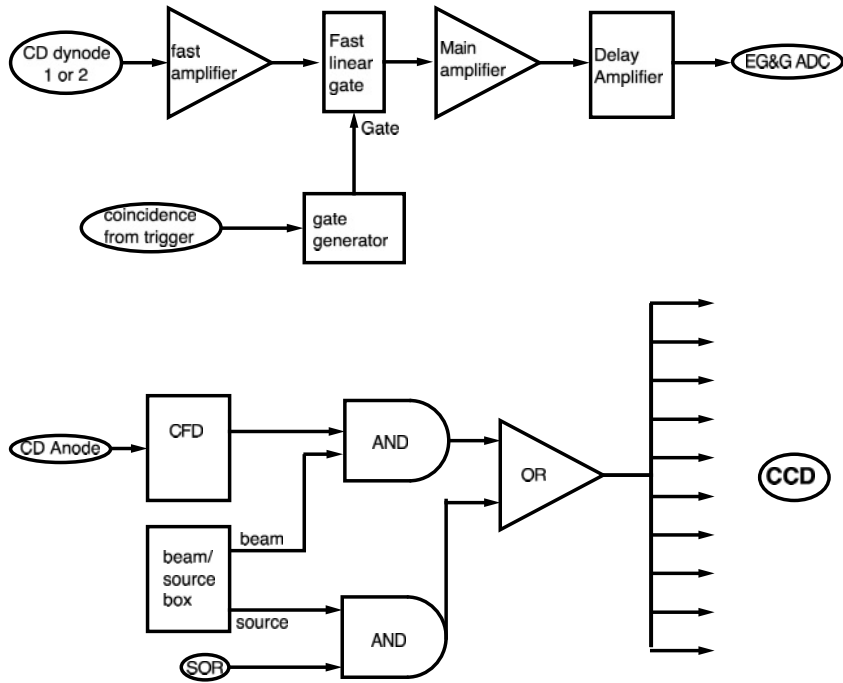


FIG. 7. Electronics diagram for the CD. Dynodes 1 and 2 denote the 10th and 11th dynode output, respectively, of a 14-stage PMT attached to the CD.

modules to select CD linear signals. The input signals for the computer trigger (see Fig. 8) consist of electronic pairs labeled P1, P2, P3, etc., where each neutron detector in a pair is in coincidence with the CD and no coincidences are required between neutron detectors forming an electronic pair (see Fig. 6). P1 through P4 are combined into a logical OR group. The same is done with P5 through P8. All triple coincidences of interest (*nn* FSI) will occur between two neutron electronic

pairs not belonging to the same logic OR group. The output signals from these two OR groups are either combined in a logical AND (for triple coincidences) or a logical OR for double coincidences. When a triple coincidence is registered, the associated coincidence signals are vetoed to avoid counting an event as both triple and double.

Because of the large rate of double events, it was necessary to implement a divide-down circuit (see Fig. 9). This is

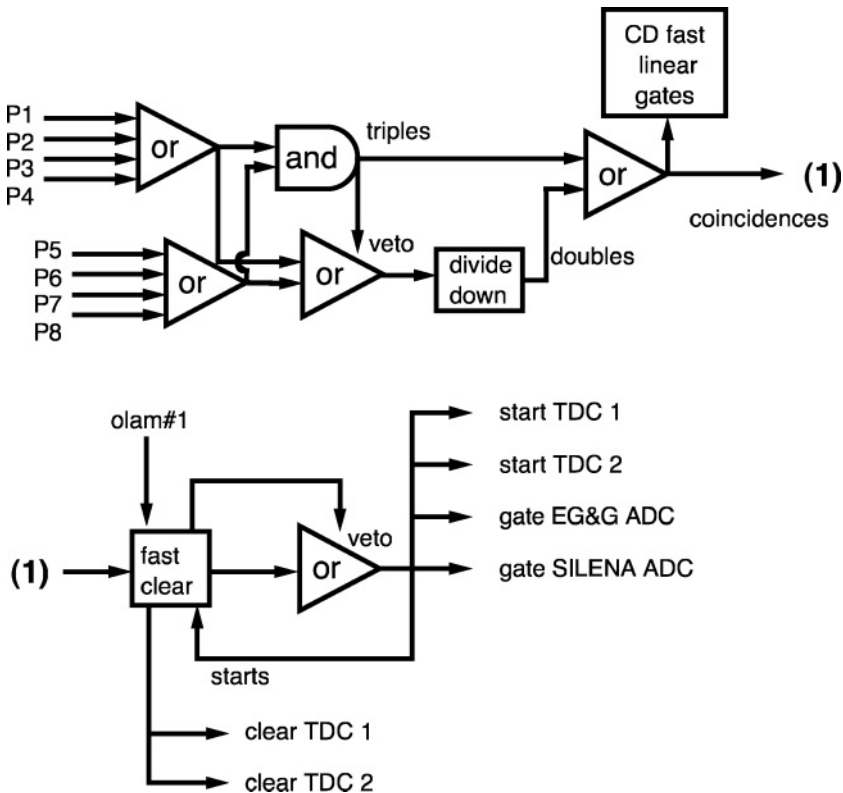


FIG. 8. Simplified computer trigger electronics diagram.



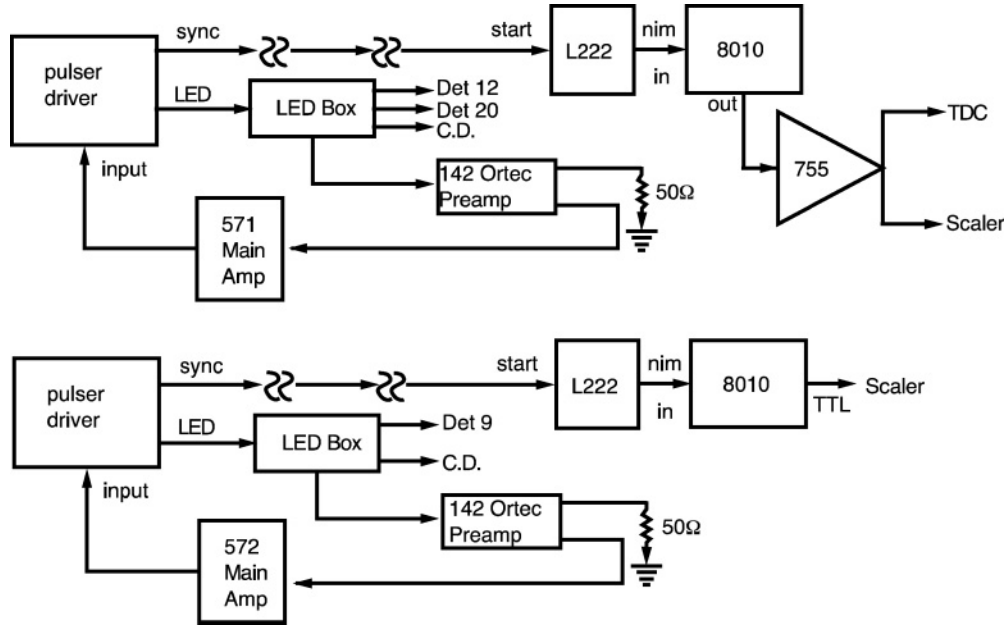


FIG. 10. LED pulser electronic diagram.

and  $\vec{q}$  and additionally specified by nucleon spin and isospin projection quantum numbers, that is,

$$|\phi_0\rangle = |\vec{p}\vec{q}m_1m_2m_3m_{t_1}m_{t_2}m_{t_3}\rangle. \quad (2)$$

The breakup transition operator

$$U_0 = (1 + P)\tilde{T} \quad (3)$$

is expressed in terms of a  $\tilde{T}$  operator which sums up all multiple-scattering contributions through the integral equation [27]

$$\begin{aligned} \tilde{T}|\phi\rangle &= tP|\phi\rangle + (1 + tG_0)V_4^{(1)}(1 + P)|\phi\rangle + tPG_0\tilde{T}|\phi\rangle \\ &+ (1 + tG_0)V_4^{(1)}(1 + P)G_0\tilde{T}|\phi\rangle. \end{aligned} \quad (4)$$

The operator  $P$  is the sum of a cyclical and anticyclical permutation of three nucleons,  $t$  is the  $NN$   $t$  matrix, and  $G_0$  is the free propagator. Equation (4) takes into account rescattering by  $NN$  and  $3N$  interactions. Mostly we use Eq. (4) for the case when only pairwise forces are active. However, to obtain information on effects caused by a  $3NF$  on the  $nn$  FSI interaction, Eq. (4) was solved also by including the  $2\pi$ -exchange Tucson-Melbourne (TM)  $3NF$  [21]. The  $3NF$  is divided into three parts,

$$V_4 = \sum_{i=1}^3 V_4^{(i)}, \quad (5)$$

where each one is symmetrical under exchange of two particles. For the  $2\pi$ -exchange  $3NF$ , for instance, this corresponds to the three possible choices of the nucleon which undergoes the (off-shell)  $\pi$ - $N$  scattering.

In the present work, Eq. (4) was solved in a partial-wave projected momentum space basis at energies relevant to the present experiment using the following  $NN$  interactions: Bonn B [3], CD Bonn [28], and Nijmegen I [29]. For the calculations with a  $3NF$ , we took the TM force with the cutoff parameter

adjusted individually together with each  $NN$  interaction (CD Bonn and NijmI) to reproduce the experimental triton binding energy value [30]. In all calculations, partial-wave states with total angular momentum in the two-nucleon subsystem up to  $j_{\max} = 3$  were taken into account. This restriction is justified for the energy of the present experiment. Calculations performed with the CD Bonn potential including  $j = 4$  force components have shown that contributions from angular momentum  $j > 3$  components to the  $nn$  FSI cross section are negligible.

Starting from the transition matrix elements, the cross sections were obtained in the standard way [18]. For details of both the underlying formalism and the numerical treatment, we refer to Refs. [17,18,30,31].

Since the aim of the present work is to determine the  $^1S_0$   $nn$  scattering length  $a_{nn}$ , the charge-dependence breaking in the  $^1S_0$   $NN$  interaction had to be included. This was accomplished in an exact way by taking the  $3N$  isospin  $T = 3/2$  admixture into account [32]. This requires different  $np$  and  $nn$   $^1S_0$  interactions. For the CD Bonn and NijmI potentials, this is automatically fulfilled because of their inherent charge dependence. The Bonn B potential is fitted in the  $^1S_0$  state to the  $np$   $^1S_0$  scattering length  $a_{np}$ . In order to determine  $a_{nn}$  from comparison of experimental data and theoretical  $nn$  FSI cross sections, one needs a set of  $nn$   $^1S_0$  interactions with particular values for  $a_{nn}$ . Modifications of the  $^1S_0$   $nn$  interaction were accomplished for the Bonn B  $NN$  potential by adjusting the value for the  $\sigma$ -meson coupling constant  $g_\sigma^2/4\pi$ . For the CD Bonn potential, the modification was achieved by adjusting the strength of the  $^1S_0$   $nn$  interaction [33]. Similarly, for the NijmI potential, it was modified by changing the strength of the diffractive part of the  $^1S_0$   $nn$  interaction [34].

Theoretical point-geometry cross-section libraries were generated for a range of  $a_{nn}$  values at the incident energies and outgoing neutron production angles of interest. These cross-section libraries formed the basis of the MC calculations

used to simulate the experiment and to determine  $a_{nn}$  from the experimental  $nn$  FSI cross-section data.

#### IV. MONTE CARLO CALCULATIONS

The experimental setup was accurately modeled for  $nd$  elastic scattering and the  $nn$  FSI breakup processes of interest using MC simulations. Here, we focus on the  $nd$  breakup process.

##### A. $nd$ breakup MC simulations

The experimental  $nd$  breakup data are affected by effects such as the finite pulse-height and time-of-flight resolution of the CD and neutron detectors, the energy-dependent efficiencies of the neutron detectors, the attenuation effects from structural materials, and the finite geometry of the neutron production gas cell, CD, and neutron detectors. Instead of trying to extract point-geometry cross sections from the experimental  $nd$  breakup data, we modeled these effects in an MC simulation of the experiment. This required the calculation of the following quantities: (a) the product of the transmission probabilities of both  $nd$  breakup neutrons detected in the neutron detectors

$$\bar{\alpha}(E_1, E_2, E_3) = \alpha_1(E_1)\alpha_2(E_2), \quad (6)$$

where  $E_1$  and  $E_2$  are the neutron energy of neutron 1 and 2, respectively, and  $E_3$  stands for the proton energy; (b) the absolute neutron detection efficiency product

$$\bar{\epsilon}(E_1, E_2, E_3) = \epsilon_1(E_1)\epsilon_2(E_2); \quad (7)$$

(c) the Gaussian-shaped proton energy distribution weight factor  $\omega(E_3)$  due to the limited pulse-height resolution of the center detector; and (d) the point-geometry theoretical differential  $nd$  breakup cross section  $\frac{d^3\sigma_{nn}^{\text{th}}}{d\Omega_1 d\Omega_2 dS}(E_1, E_2, E_3)$ .

Extensive ( $\sim 10^5$  individual values) theoretical  $nd$  breakup differential cross-section libraries were created for the  $nn$  FSI configuration of interest. These libraries were required to span the finite geometry of the experimental setup and the energy spread of the incoming neutron beam. Differential cross sections were generated along kinematic  $S$  curves for breakup configurations determined by the  $nn$  production angles  $\theta_1, \theta_2, \phi_{12}$ , and the incoming neutron beam energy  $E_n$ . The cross sections were calculated as a function of  $S$  curve length in steps of 0.1 MeV, always starting at the point where  $E_2 = 0$  MeV.

The energies of the outgoing neutrons are experimentally determined from their time-of-flight, where it is assumed that the neutrons travel from the geometric center of the CD to the center of the neutron detectors. To directly compare experimental and MC results, it is necessary to express the MC output as a function of kinetic energies

$$E_3 = E_{\text{tot}} - E_1 - E_2, \quad (8)$$

where  $E_{\text{tot}}$  is the total kinetic energy available to the three nucleons in the outgoing channel (10.775 MeV for an  $E_n = 13.0$  MeV neutron beam), and

$$E'_i = (d_i^2/d_i^2)E_i, \quad (9)$$

with  $i = 1$  or 2. The center-to-center distance from the target to the neutron detector is  $d'_i$ , and  $d_i$  is the actual distance traveled by the simulated neutron. For the proton, we have  $E'_3 = E_3$ .

The  $nd$  breakup MC output for a simulated event is generated in the following way:

- (i) Points are randomly selected within the deuterium gas cell, CD, and pair of neutron detectors in an  $nn$  FSI configuration. This choice fixes the angles  $\theta_1, \theta_2, \phi_{12}$ , while the incoming neutron energy  $E_n$  is chosen from the nearly rectangular distribution between 12.8 and 13.2 MeV, determining a kinematic locus  $S(E_1, E_2, E_3)$ .
- (ii) The theoretical cross-section libraries are used as a basis for a multiparameter interpolation to obtain the  $nn$  FSI cross section as a function of  $S$  curve length. The interpolation parameters used are  $\theta_1, \theta_2, \phi_{12}, E_n$ , and the breakup nucleon momenta  $k_1, k_2$ , and  $k_3$ .
- (iii) The values for  $\bar{\epsilon}(E_1, E_2, E_3)$ ,  $\bar{\sigma}(E_1, E_2, E_3)$ ,  $\bar{\alpha}(E_1, E_2, E_3)$ , and  $\omega(E_3)$  are calculated for each point on the MC event's  $S$  curve. Here,  $\bar{\sigma}(E_1, E_2, E_3)$  is the theoretical  $nd$  breakup differential cross section obtained after interpolation using the cross-section libraries. The individual neutron detector efficiencies  $\epsilon_1(E_1)$  and  $\epsilon_2(E_2)$  are introduced in the MC code by means of data tables.
- (iv) The weight factor elements  $\kappa(E'_1, E'_2, E'_3)$  are given by

$$\kappa(E'_1, E'_2, E'_3) = \omega(E_3)\bar{\alpha}(E_1, E_2, E_3)\bar{\epsilon}(E_1, E_2, E_3). \quad (10)$$

Likewise, the cross section elements  $s(E'_1, E'_2, E'_3)$  are given by the product

$$s(E'_1, E'_2, E'_3) = \bar{\sigma}(E_1, E_2, E_3)\omega(E_3)\bar{\alpha}(E_1, E_2, E_3) \times \bar{\epsilon}(E_1, E_2, E_3). \quad (11)$$

The finite-geometry theoretical  $nd$  breakup differential cross sections  $\frac{d^3\sigma_{nn}^{\text{MC}}}{d\Omega_1 d\Omega_2 dS}(S)$  are obtained through the following procedure:

- (i) The point-geometry locus  $S(E_1^c, E_2^c, E_3^c)$  is obtained for the  $nn$  FSI configuration in steps of  $\Delta S = 0.5$  MeV (superscript  $c$  denotes the ideal point-geometry locus). The locus  $S, \kappa$ , and  $\bar{\Sigma}$  are reindexed in terms of the momenta

$$k'_i = \sqrt{2E'_i m}, \quad (12)$$

where  $i = 1, 2, 3$ . The mass of the proton and neutron are taken to be identical ( $m = 939$  MeV).

- (ii) The value for each element  $\kappa(k'_1, k'_2, k'_3)$  and  $s(k'_1, k'_2, k'_3)$  is assigned to a point on the  $S(k'_1, k'_2, k'_3)$  curve, where the momentum space distance

$$K = \sqrt{\sum_{i=1,2,3} (k'_i - k'_i)^2} \quad (13)$$

is minimized [35]. From these projections we obtain the simulated yield curve and the weight factor curve

$$\bar{\Sigma}(S) = \frac{\sum_{k'_i} s(k'_1, k'_2, k'_3)}{\sum_{k'_3} \omega(k'_3)} \quad (14)$$

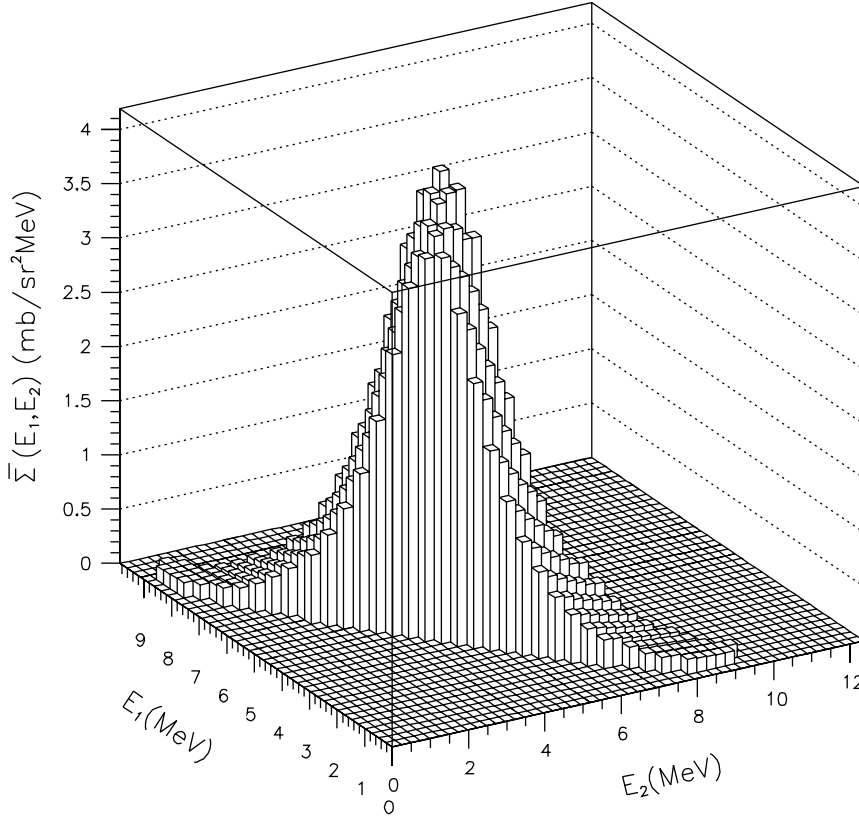


FIG. 11. MC generated  $\bar{\Sigma}(E'_1, E'_2, E'_3)$  matrix projected onto the  $E'_1$ - $E'_2$  plane for  $\theta_{nn} = 20.5^\circ$ . This finite geometry calculation uses the results of rigorous  $3N$  calculations based on the Bonn B  $NN$  potential model.

and

$$\kappa(S) = \frac{\sum_{k'_i} \kappa(k'_1, k'_2, k'_3)}{\sum_{k'_i} \omega(k'_3)}. \quad (15)$$

The summations go over the indices  $k'_i$  that correspond to a point  $S$  on the ideal  $S$  curve according to the criterion given by Eq. (13).

(iii) Finally, the expression

$$\frac{d^3 \sigma_{ann}^{MC}}{d\Omega_1 d\Omega_2 dS}(S) = \frac{\bar{\Sigma}(S)}{\kappa(S)} \quad (16)$$

yields the finite-geometry theoretical  $nd$  breakup differential cross section for discrete values of  $S$  along the ideal  $nn$  FSI kinematic locus  $S(E_1^c, E_2^c, E_3^c)$  (see Fig. 11). The subscript  $ann$  indicates the neutron-neutron scattering length corresponding to the library used in the cross-section calculation. Thus, the point-geometry theoretical and experimental  $nn$  FSI cross-section curves can be compared directly (see Fig. 12).

## V. DATA ANALYSIS

Data were partially sorted online in order to monitor essential experimental parameters such as the neutron and center detector PHs, the TOFs for double and triple events, and the PSDs for all detectors. The online sorting was kept to a minimum in order to reduce the dead time of the data-acquisition system, which was mostly due to the computer.

Two-dimensional plots of yields in  $E_1$  versus  $E_2$  space were created online to ensure that the  $nn$  FSI yields were indeed occurring around the ideal loci. These distributions of  $nn$  FSI yields became evident for all four configurations only after about one day of data accumulation.

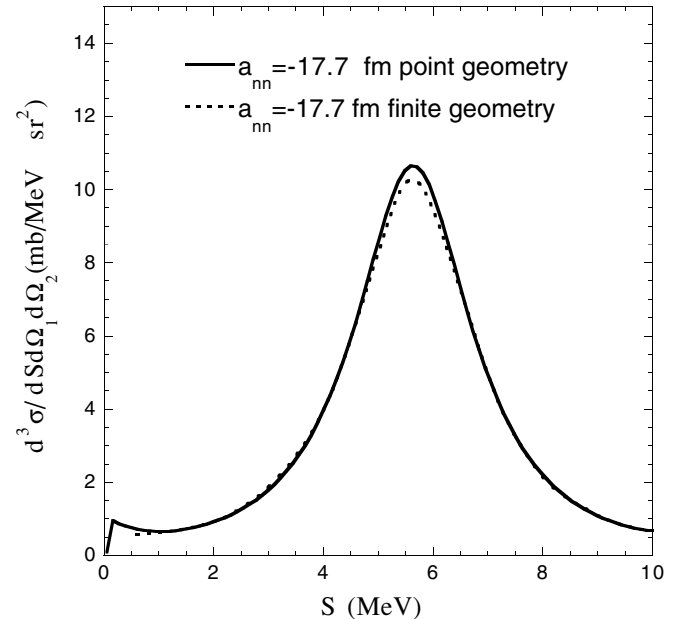


FIG. 12. Comparison of point-geometry and finite-geometry differential  $nd$  breakup cross sections for  $\theta_{nn} = 28.0^\circ$  using the Bonn B  $NN$  potential model with  $a_{nn} = -17.7$  fm.

The data sorting was divided into two parts:

- (i) Double events were sorted to find the yields from  $nd$  elastic scattering, and to extract the luminosity  $\beta_r$  for a particular run. In this way the  $nd$  breakup yields from each of our seven runs could be normalized for later determination of the  $nn$  FSI cross section.
- (ii) Triple events were sorted to find the  $nd$  breakup yields corresponding to each  $nn$  FSI configuration and to obtain absolute cross sections from these yields. The triple events had to satisfy the total-energy requirement (in MeV)

$$6.77 \leq E_t = E_1 + E_2 + E_3 \leq 10.77. \quad (17)$$

This fairly large energy range was necessary because of the limited energy resolution of the CD. Furthermore, the triple events had to fulfill the kinematic requirement

$$E_{\min}\{E_1, E_2\} \leq E_{\text{el}}, \quad (18)$$

where  $E_{\min} = 0.4$  MeV and  $E_{\text{el}}$  is the energy of neutrons that scatter elastically from deuterons in the CD to the neutron detectors forming the  $nn$  FSI configuration of interest.

## A. Elastic $nd$ scattering

### 1. Luminosity determination

The determination of the absolute  $nn$  FSI cross section from the measured data requires the measurement of the luminosity, defined as

$$\beta_r = \frac{N_n^r N_d}{Q_r}, \quad (19)$$

where  $N_n^r$  is the number of neutrons incident on the CD during a particular run  $r$ ,  $N_d$  is the density of deuterium atoms in the CD, and  $Q_r$  is the charge deposited by the deuteron beam in the deuterium gas cell during run  $r$ . The luminosity was determined from the  $nd$  elastic scattering yield  $Y_{\text{el}}^r(\theta)$  by

$$Y_{\text{el}}^r(\theta) = \frac{d\sigma_{\text{lab}}}{d\Omega}(\theta) \alpha(E_n, E_{\text{el}}) \epsilon(E_{\text{el}}) \beta Q_r \Omega, \quad (20)$$

where  $\alpha(E_n, E_{\text{el}})$  is the transmission probability of  $nd$  elastically scattered neutrons with incident energy  $E_n$  and energy  $E_{\text{el}}$  after elastic scattering, taking into account the building materials of the CD, and including air attenuation between the CD and the neutron detector of interest. The absolute detection efficiency of the neutron detector for neutrons with energy  $E_{\text{el}}$  is  $\epsilon(E_{\text{el}})$ , and the solid angle subtended by the neutron detector is  $\Omega$ . The values for the  $nd$  elastic scattering differential cross section in the lab frame  $\frac{d\sigma_{\text{lab}}}{d\Omega}(\theta)$  were taken from Ref. [36].

The yield  $Y_{\text{el}}^r(\theta)$  was determined from the center detector pulse-height (CDPH) spectrum generated by placing a gate around the TOF peak due to  $nd$  elastically scattered neutrons (see Fig. 13). The determination of  $Y_{\text{el}}^r(\theta)$  requires the subtraction of counts due to accidental, multiple scattering (MS), and correlated backgrounds. The contribution of accidentals can be estimated by setting a gate in the TOF spectrum before the  $\gamma$ -ray peak (not visible in Fig. 13 because of the PSD constraint), where no truly correlated events can exist. This gate has the same width as the gate used for the  $nd$  elastic

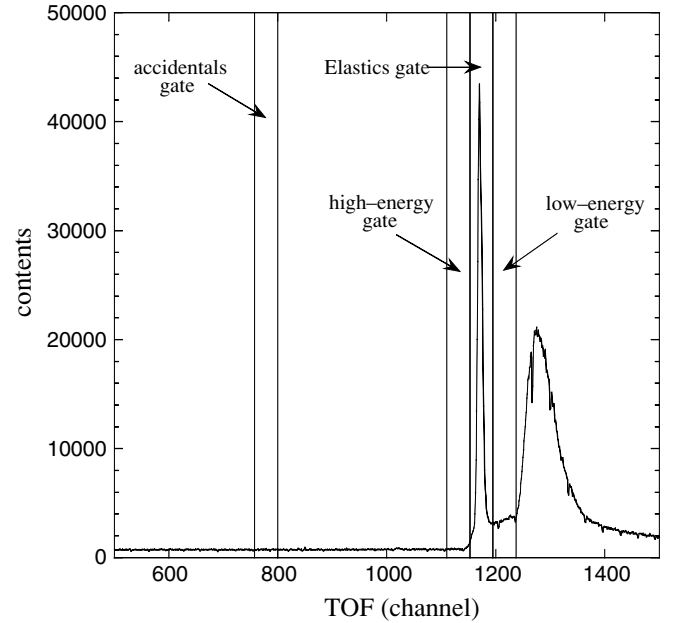


FIG. 13. TOF spectrum for neutron scattering from the CD to neutron detector 8 (“doubles” spectrum). Time increases from left to right. The pronounced peak below channel 1200 is due to elastic scattering of neutrons produced in the deuterium gas cell by deuteron breakup reactions. A  $\gamma$ -ray peak is not visible because of the applied  $n$ - $\gamma$  pulse-shape discrimination. The time resolution is 0.2 ns/channel.

scattering events. The accidentals are then sorted in the same way as the events within the elastic scattering event’s TOF gate, generating an accidental’s CDPH spectrum.

The  ${}^2\text{H}(d, n){}^3\text{He}$  reaction used in the present experiment to produce 13.0 MeV neutrons also creates a continuum of lower-energy neutrons via breakup of deuterons in the Havar foil and deuterium gas and on the gold beam stop of the deuterium gas cell. These so-called gas-cell breakup neutrons are lower in energy (by at least 5.5 MeV), but can scatter from a carbon nucleus and subsequently from a deuteron in the CD, such that some of them arrive at the neutron detector with the same TOF as a 13.0 MeV neutron that scattered only once from a deuteron in the CD. These scattered gas-cell breakup neutrons form a CD-correlated background beneath the  $nd$  elastic TOF peak. In addition, neutrons produced by the  $nd$  breakup reaction in the CD may also undergo scattering from carbon and arrive with a TOF indistinguishable from that of the  $nd$  elastically scattered neutrons of interest, forming also a CD-correlated background. These backgrounds were calculated by combining information from Monte Carlo simulations and experimental CDPH events from the two gates adjacent to the elastic scattering peak gate in the TOF spectrum (see low- and high-energy gates shown in Fig. 13). The CDPH spectra were generated for events falling within these gates and stored in separate data areas, and their accidental backgrounds were subtracted (see Fig. 14).

First, the experimental  $nd$  elastic TOF peaks were simulated assuming single-scattering  $nd$  elastic processes. The input parameters of the simulation were adjusted to reproduce the centroid position and the full width at half maximum (FWHM)

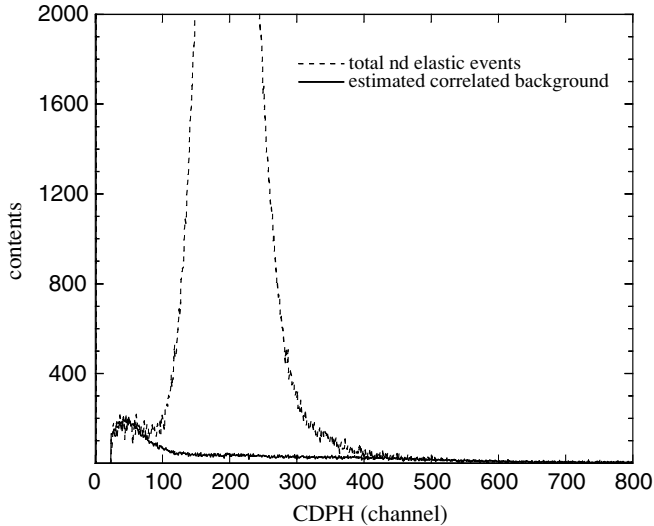


FIG. 14. Elastic scattering events (dashed curve) CDPH spectrum for neutron scattering to detector 8 after subtraction of measured accidental and calculated multiple-scattering events. The solid curve is the sample correlated background estimated from averaging the net CDPH spectra for events from the low- and high-energy TOF gates (see Fig. 13) on either side of the peak of interest (after corrections for accidental and multiple scattering events). The resulting spectrum is normalized to match the high-PH region and the beginning of the elastic scattering PH enhancement.

of the experimental  $nd$  elastic TOF peak. In addition, the MC generated CDPH spectrum associated with  $nd$  elastic scattering events was matched to the shape and area of the experimental CDPH spectrum (with accidental events already subtracted). This was accomplished after calculating an exponential background under the experimental CDPH deuteron-recoil peak, matching the region to the left of the peak and the high PH tail to the right of the peak. The calculated background was then subtracted from the experimental CDPH, and the input parameters of the MC simulation were modified to reproduce the net CDPH spectrum. The MC  $nd$  elastic simulations for multiple-scattering (MS) events described below could then be properly normalized and subtracted from the CDPH experimental spectra for events falling in the  $nd$  elastic, low- and high-energy TOF gates (see Fig. 13).

The second step consisted of calculating the MS contributions. The MS events originated from neutrons that scattered multiple times from carbon and deuterium nuclei of the CD into a neutron detector. Only neutron double scattering was of significance in this experiment. Therefore, we simulated in our MC calculation only deuteron-deuteron, deuteron-carbon, and carbon-deuteron neutron double scattering contributions to the TOF and PH spectra. Double scattering of neutrons involving two carbon nuclei (in our notation: carbon-carbon) was not considered since it leaves no detectable signal in the CD. The simulated MS contributions were normalized and subtracted from their corresponding experimental CDPH spectra. The resulting CDPH spectra belonging to the low- and high-energy TOF gates were averaged channel-by-channel and normalized to fit the tail-end and low-PH parts of the CDPH spectrum derived from events within the elastic

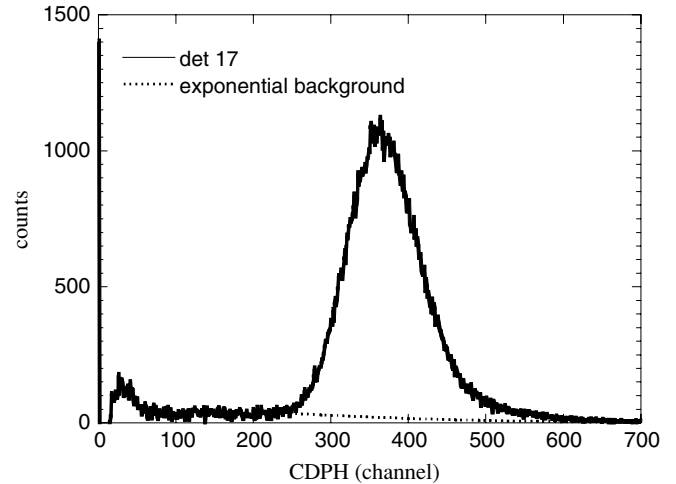


FIG. 15. CDPH spectrum for elastic scattering to neutron detector 17.

scattering TOF gate (see Fig. 14). After subtraction of this averaged spectrum, a small residual background remained. This can be seen more clearly in the CDPH spectra obtained for larger  $nd$  scattering angles (see Fig. 15). Typically, this residual background was a few percent of the elastic scattering events and included processes that were not simulated in the present MC calculations (for example, multiple scattering events involving deuterium and the glass container of the CD or the PMT), but were understood from previous MC simulations performed by our group for other experiments. An exponential fit was made of this sample-correlated residual background (dotted curve in Fig. 15) and subtracted from the elastic's CDPH spectrum. The resulting net CDPH spectrum was integrated between the channels where the calculated background met the experimental CDPH spectrum in the low-PH end, and up to the end of the experimental CDPH spectrum. Thus, we obtained the net elastic scattering yield  $Y_{el}^r(\theta)$  for a particular  $nd$  elastic scattering angle and run.

The  $nd$  elastic yields were determined for at least three neutron detectors (typically detectors 8, 17, and 18) for a given run to check for systematic uncertainties in the extraction of  $Y_{el}^r(\theta)$ . The percent standard deviation from the mean luminosity  $\beta_r$  varied between 0.5% and 2.6% for our seven runs.

## 2. Dead-time and ADC-loss corrections

As indicated already in Sec. II B 3, dead-time correction (DTC) factors were determined using LED and electronic pulsers. The electronic signals generated by each pulser driver were sent to scalars and counted by the computer. Most of the dead time of the system was incurred by the computer in processing the data and vetoing further incoming trigger signals until it was ready to register the next event. This was tested by independent LED and electronic pulsers.

Two LED pulsers were coupled to the CD. One of them "fired" neutron detector 12 and the other fired neutron detector 20, correlating events for every pulse and forcing them to go through the triple-coincidence part of the trigger circuit. It was made sure that the LED pulses always satisfied the threshold

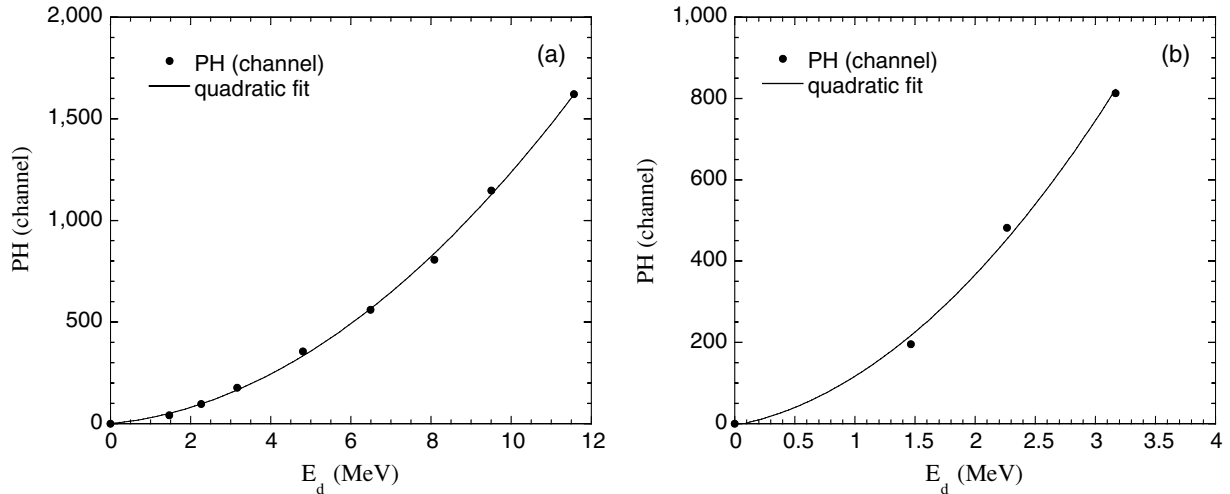


FIG. 16. Light-output functions for deuterons of CD using (a) dynode 10 low-gain output and (b) dynode 11 high-gain output. Solid curves are fits to the data.

and PDS requirements. Thus, pulser events were lost mostly to dead time.

Every LED pulser event was tagged in the computer by sending the pulser driver's electronic signal to a TDC channel. The pulser events were then selected using the tag and accumulated in separate PH, PSD, and TOF spectra. To obtain the DTC, the number of LED pulser driver hits counted in the scaler were divided by the number of LED pulser events registered by the computer.

An electronic pulser sent signals directly to the TDC channels used for TOF and PSD, to the trigger circuit that provided start signals, and to a scaler. A TDC channel was used for tagging. The pulser signal was also sent to the neutron detector preamplifiers to allow PH analysis. The DTC was calculated as in the case of the LED pulser. Both electronic and LED pulsers gave DTCs that agreed within  $\pm 0.005$ . For most detectors, the DTCs were  $\sim 1.06$ . The triple-event DTC for a pair of detectors in an  $nn$  FSI configuration was given by whichever detector in the pair had the largest doubles DTC.

Sometimes an ADC would trigger on a false peak signal causing a zero PH count to be recorded instead of the true linear signal. This type of "misfire" was random and accumulated in the zero channel of the PH spectrum. These ADC losses were measured by taking the ratio of zero-channel counts to the total number of counts in the PH spectrum for each detector. The ADC losses were  $\sim 2\%$ . The LED pulser was used to confirm the ADC losses calculated from the PH spectra.

### 3. Center detector light output

Kinematically overdetermined measurements are possible through the detection of signals from the two neutrons and the associated proton from the  $nd$  breakup process. In our case, the proton light output in the CD is needed to determine the proton energy. The CDPH spectra associated with  $nd$  elastic scattering to the neutron detectors were used to establish the deuteron light-output function  $L_d(E)$  for high and low CDPH gains (see Fig. 16). The light-output functions for protons

$L_p(E)$  were determined using the expression [37]

$$L_p(E) = \frac{1}{2}L_d(2E), \quad (21)$$

allowing us to calculate the proton energy from the pulse height in the CD for protons associated with the neutrons detected in  $nn$  FSI events.

## B. $nd$ breakup

### 1. Breakup event sorting

Neutron-deuteron breakup events were identified using a series of PH, PSD, and kinematic requirements on the experimental data stored on tape. These software cuts reduced the breakup data to be stored on summary tapes by a factor of 10 000. Only events belonging to the four  $nn$  FSI configurations studied were written onto summary tapes. Each breakup event had to exceed the neutron PH thresholds of  $1/3 \times Cs$ , satisfy the PSD requirements, have a proton energy of greater than 0.4 MeV, and fall within the total energy window of  $10.775 \pm 4.0$  MeV. The energy of both neutrons in an event were calculated from their TOFs, and the proton energy was established from the light-output function(s)  $L_p(E)$ .

The accepted triple events consisted of the following parameters: Configuration number, event-type tag (true+accidental or accidental, see below), TOFs of both neutrons, low- and high-gain CDPH, and neutron and proton energies. All events written on summary tapes were converted to  $n$ -tuples for analysis using the PAW (Physics Analysis Workstation) software package.

The TOFs for a neutron detector (see Fig. 17) may fall within either of two possible gates: Accidental (A) or true+accidental (T+A). For experimental and instrumental reasons, the A gate could not be made as wide as the T+A gate, making the accidental background subtraction for breakup events a little bit more complicated. We made the A gate half as wide as the T+A gate. Accidental events do not have a real TOF (and energy) associated with them, but since they are randomly distributed throughout the TOF spectrum,

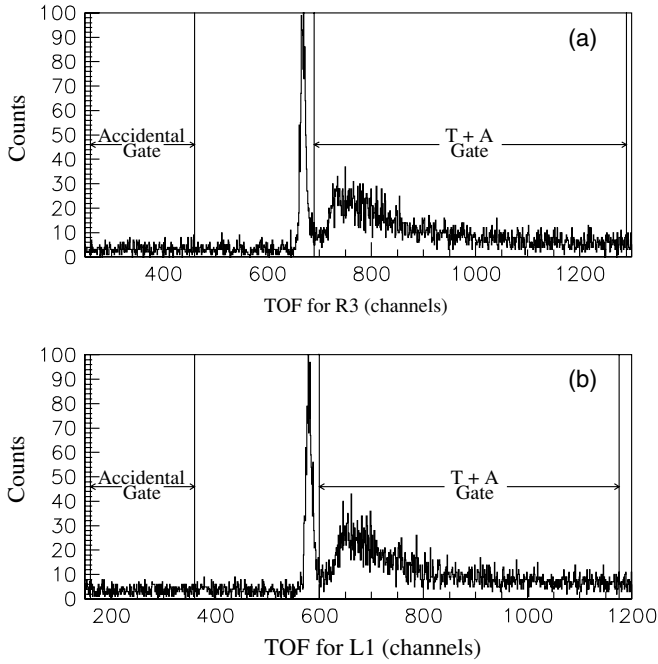


FIG. 17. Typical “triples” neutron time-of-flight spectra for detectors (a) 6 (R3) and (b) 17 (L1) showing accidental (A) and true+accidental (T+A) gates.

one can assign them a TOF in the following way. If an event has a TOF that falls within the T+A gate and another TOF falling in channel  $c$  within the accidental gate, then that event is assigned a TOF channel  $c' = (c - c_a) + c_{t+a}$ , where  $c_a$  is the first channel of the accidental gate and  $c_{t+a}$  is the first channel of the T+A gate. Because the accidental gate is only one-half the width of the T+A gate, an additional event is generated with TOF channel

$$c' = (c - c_a) + c_{t+a} + \frac{\Delta C_{t+a}}{2}, \quad (22)$$

where  $\Delta C_{t+a}$  is the width of the T+A gate. If both TOFs in an event fall within the accidental gates, then four events are generated with TOFs given by the procedure described above.

## 2. Breakup cross-section determination

Breakup events for each  $nn$  FSI configuration were indexed according to the momenta of the neutrons and the proton. Accidental events were treated in the same way but separately from true+accidental events for later subtraction. The ideal point-geometry locus for a given  $nn$  FSI configuration was discretized in steps of 0.5 MeV, and each point on the  $S$  curve had its associated energies ( $E_1^c, E_2^c, E_3^c$ ) converted into momenta ( $k_1^c, k_2^c, k_3^c$ ). In order to obtain yields as a function of  $S$ -curve length, we projected the experimental points in momentum space ( $k_1^{\text{exp}}, k_2^{\text{exp}}, k_3^{\text{exp}}$ ) onto the ideal kinematic locus points nearest to them by varying ( $k_1^c, k_2^c, k_3^c$ ) until minimizing the distance in momentum space [35]

$$K = \sqrt{\sum_{i=1,2,3} (k_i^c - k_i^{\text{exp}})^2}. \quad (23)$$

A neutron from the incident neutron beam can scatter off the CD, causing a recoil deuteron to produce a detectable signal. The same neutron can then proceed to interact with the ring detector of an  $nn$  FSI configuration via multiple scattering (single scattering off a proton or a carbon nucleus in the ring detector will not produce a signal above the PH threshold of  $1/3 \times Cs$ ) and then interact with the back detector of the same  $nn$  FSI configuration. This type of event is in principle indistinguishable from a true  $nd$  breakup event. Usually, the energy deposited by such events in the CD is below our detection threshold, but because of the CDPH pile-up due to  $\gamma$  rays and the continuum of gas-cell breakup neutrons, the pulse height may exceed our CD threshold.

Another type of cross-talk events comes from true  $nd$  breakup processes where the proton is detected in the CD, one neutron leaves in an unspecified direction, and the second neutron is detected via multiple scattering in a ring detector and subsequently in its associated Bicron detector.

Partly because of their large kinematic range, cross-talk events are smoothly distributed in ( $E_1, E_2, E_3$ ) space or associated momentum space. In order to estimate the contribution of the cross talk to the raw  $nn$  FSI yields, every event that was projected onto its closest point on the ideal  $S$  curve was also assigned to a point  $E_h = E_1 + E_2$  in a diagonal projection histogram (DPH) binned in steps of 0.1 MeV. Every point on the ideal  $S$  curve for every  $nn$  FSI configuration had a corresponding DPH. This is equivalent to projecting events corresponding to a point on the ideal  $S$  curve onto the line  $E_1 = E_2$ . The diagonal projections consist of a prominent  $nn$  FSI enhancement [as expected from Figs. 5(a)–5(d)] with a smooth background of cross-talk events (see Fig. 18). The experimental DPHs for each run were averaged according to the expression

$$\bar{Y}_{\text{raw}}(E_h, S) = \frac{1}{R} \sum_r \frac{Y_r(E_h, S) k_r^{\text{DTC}}}{\beta_r Q_r}, \quad (24)$$

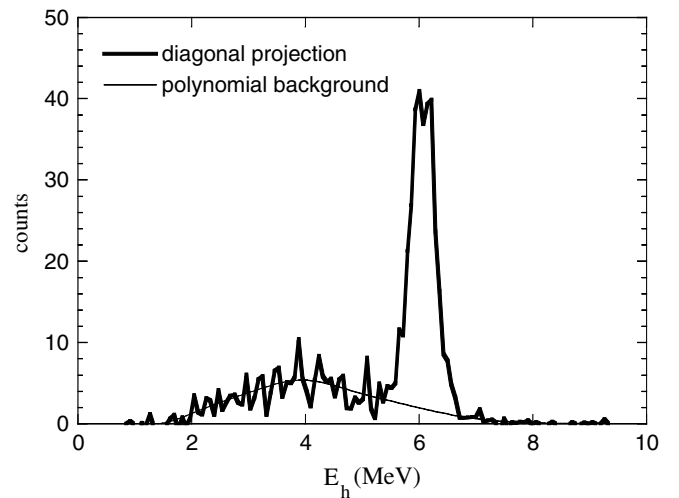


FIG. 18. Diagonal projection of experimental data for the  $nn$  FSI configuration at  $\theta_{nn} = 20.5^\circ$ .  $E_h$  is the sum of the two neutron energies. The cross-talk background under the  $nn$  FSI peak is fitted by a fifth-degree polynomial.

where  $Y_r(E_h, S)$  are the raw yields projected onto the  $E_1 = E_2$  diagonal for a particular run,  $\beta_r$  is the luminosity,  $Q_r$  is the charge deposited by the incident deuteron beam in the deuterium gas cell,  $k_r^{\text{DTC}}$  is the triple dead-time correction factor, and  $R$  is the total number of runs. The experimental diagonal projections  $\bar{Y}_{\text{raw}}(E_h, S)$  were fitted by a MC simulated DPH curve (multiplied by a normalization factor) plus a fifth-order polynomial to model the background directly underneath and around the  $nn$  FSI peak. The polynomial curve was then subtracted from the experimental DPH, and the remaining distribution was integrated using the limits provided by the MC simulation of the DPH, thus obtaining the net average yield as a function of  $S$ -curve length  $\bar{Y}_{\text{net}}(S)$  for each  $nn$  FSI configuration. The differential  $nd$  breakup cross section as a function of  $S$ -curve length was calculated using the expression

$$\frac{d^3\sigma(S)}{d\Omega_1 d\Omega_2 dS} = \frac{\bar{Y}_{\text{net}}(S)}{\kappa(S)\Omega_1\Omega_2\Delta S}, \quad (25)$$

where  $\Delta S = 0.5$  MeV,  $\Omega_i$  are the solid angles subtended by the detectors used in a  $nn$  FSI configuration, and  $\kappa(S)$  are the MC calculated attenuation and efficiency factors.

### 3. Breakup cross-section uncertainties

The systematic uncertainties associated with the experimental  $nd$  breakup cross sections have several sources.

- (i) The uncertainties in the solid angles  $\Omega_1$  and  $\Omega_2$  (0.67%, 0.4%) are due to the uncertainty in the distance of the neutron detectors from the CD and the uncertainty in the radii of the ring detectors. These solid angle errors are assumed to have a normal distribution.
- (ii) The systematic uncertainty in the neutron detection efficiency of each detector is partly due to the normalization to the  ${}^2\text{H}(d, n){}^3\text{He}$  reaction cross section [38]. This normalization uncertainty ( $\pm 1.5\%$ ) has the same sign and magnitude for all detectors. In addition, there is some uncertainty  $\Delta\epsilon^R$  in the efficiency due to uncertainties in distance measurements, deuterium pressure in the gas cell, beam heating effects, etc. The latter error ( $\pm 1\%$ ) is assumed to have a normal distribution.
- (iii) The attenuation factors  $\alpha_i$  have a normalization uncertainty of  $\pm 1.5\%$  due to the associated neutron total cross-section uncertainties.
- (iv) The systematic uncertainty in the luminosity  $\beta_r$  is partly caused by the  $nd$  elastic scattering differential cross-section uncertainty ( $\pm 1.5\%$ ). The efficiency and attenuation errors in  $\beta_r$  are taken to have the same sign and magnitude as in the  $nd$  breakup case.

The systematic uncertainty of the  $nd$  breakup cross section follows from Eqs. (25) and (20), where the normalization uncertainties from all sources were added linearly. In the final calculation of the systematic uncertainty, cancellations occur between some uncertainties because of their presence in the numerator and denominator of Eq. (25).

The systematic uncertainties which were assumed to obey a normal distribution were added in quadrature. Finally, the sums of randomly distributed uncertainty components  $(\frac{\Delta\sigma}{\sigma})^R$  and the purely systematic ones  $(\frac{\Delta\sigma}{\sigma})^S$  were added in quadrature. The

resulting total uncertainty due to systematic uncertainties is  $\pm 5\%$ . The statistical uncertainty was calculated for each point on the ideal  $S$  curve and found to be less than  $\pm 5\%$  for all cross-section maxima.

## VI. DETERMINATION OF $a_{nn}$

The neutron-neutron scattering length  $a_{nn}$  was determined from the absolute  $nn$  FSI cross-section and also from the shape of the  $nn$  FSI cross-section distribution. The latter procedure was used in all previous analyses.

### A. Determination from the absolute $nn$ FSI cross section

Finite-geometry  $nn$  FSI cross-section curves ( $\frac{d^3\sigma_{nn}^{\text{MC}}(S)}{d\Omega_1 d\Omega_2 dS}$ ) were generated by MC simulations for all configurations and for values of  $a_{nn}$  between  $-17.0$  and  $-20.0$  fm. The  $\chi^2$  value for a measured  $nn$  FSI configuration and theoretical cross-section curve is given by

$$\chi^2(a_{nn}) = \sum_S \frac{\left( \frac{d^3\sigma_{nn}^{\text{MC}}(S)}{d\Omega_1 d\Omega_2 dS} - \frac{d^3\sigma(S)}{d\Omega_1 d\Omega_2 dS} \right)^2}{\left( \Delta \frac{d^3\sigma(S)}{d\Omega_1 d\Omega_2 dS} \right)^2}, \quad (26)$$

where  $\Delta \frac{d^3\sigma(S)}{d\Omega_1 d\Omega_2 dS}$  is the statistical uncertainty associated with the experimental cross section  $\frac{d^3\sigma(S)}{d\Omega_1 d\Omega_2 dS}$ . This function was fitted for each particular  $nn$  FSI configuration by a quadratic polynomial whose minimum  $\chi_{\text{min}}^2$  gives the value for  $a_{nn}$  (see Fig. 19). The statistical uncertainty of this  $a_{nn}$  determination is given by

$$\Delta a_{nn}^{\text{stat}} = |a_{nn}(\chi_{\text{min}}^2) - a_{nn}(\chi_{\text{min}}^2 + 1)|. \quad (27)$$

To estimate the effect of the cross section's systematic uncertainty on  $a_{nn}$ , the experimental cross sections were multiplied by 1.05 (0.95) to determine the  $a_{nn}^{\text{max}}$  ( $a_{nn}^{\text{min}}$ ) value corresponding to the new minimum in  $\chi^2$ . For each  $nn$  FSI configuration, the systematic uncertainty for  $a_{nn}$  was obtained

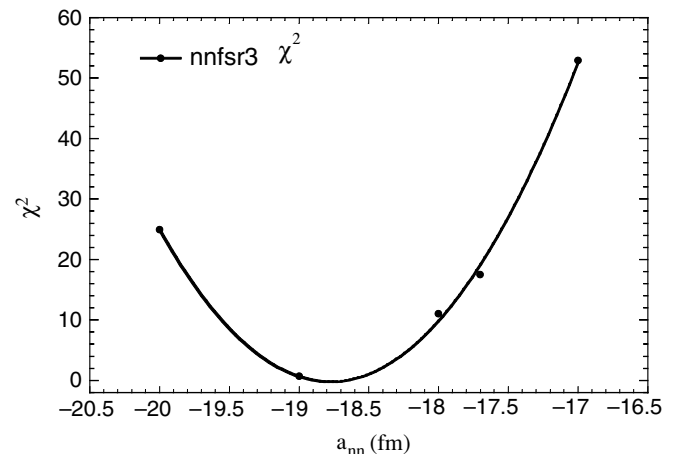


FIG. 19.  $\chi^2$  determination of  $a_{nn}$  from the absolute cross-section measurement for the  $nn$  FSI configuration at  $\theta_{nn} = 35.5^\circ$ .

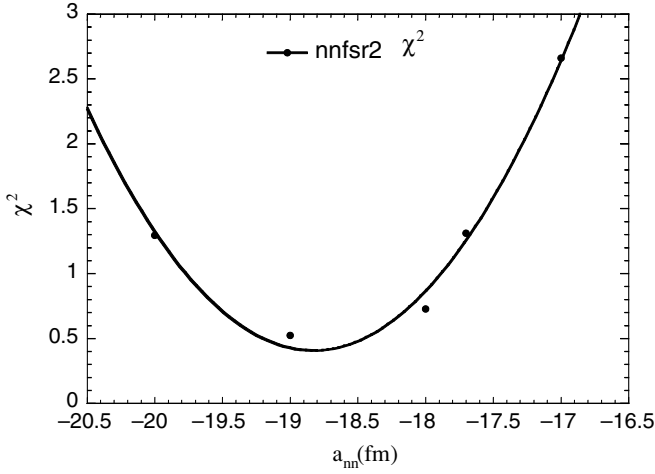


FIG. 20.  $\chi^2$  vs  $a_{nn}$  from the cross-section shape for the  $nn$  FSI configuration at  $\theta_{nn} = 35.5^\circ$ .

from

$$\Delta a_{nn}^{\text{sys}} = \frac{1}{2} (|a_{nn}^{\text{min}} - a_{nn}^{\text{max}}|). \quad (28)$$

### B. Determination from the shape of the $nn$ FSI cross section

Attempts have been made in the past to determine  $a_{nn}$  solely from the shape of the cross section using the Watson-Migdal model [12] or theoretical cross sections obtained with separable,  $S$ -wave  $NN$  potentials [10,11]. Here we applied a similar approach, but using instead rigorous Faddeev predictions of three modern  $NN$  potential models.

For each of the  $nn$  FSI configurations, the experimental cross section was multiplied by a normalization factor  $F_N$ ,

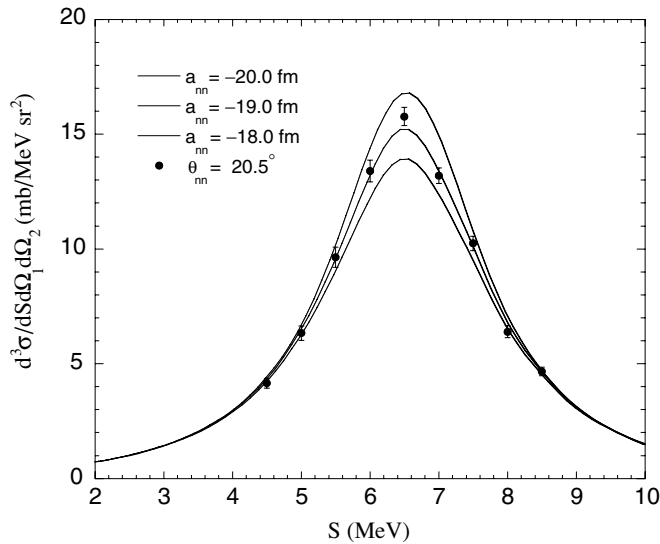


FIG. 21. Comparison of measured  $nn$  FSI cross section for  $\theta_{nn} = 20.5^\circ$  and  $3N$  calculations using different values for  $a_{nn}$ . Curves with the largest and smallest cross sections correspond to  $a_{nn} = -20.0$  fm and  $a_{nn} = -18.0$  fm, respectively. The calculations employ the  $^1S_0$  modified Bonn B  $NN$  potential model.

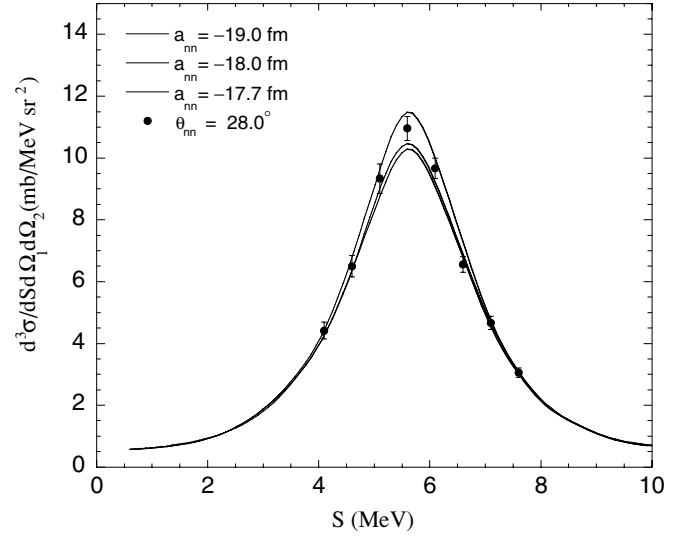


FIG. 22. Same as Fig. 21, but for  $\theta_{nn} = 28.0^\circ$ . Curves with the largest and smallest cross sections correspond to  $a_{nn} = -19.0$  fm and  $a_{nn} = -17.7$  fm, respectively.

taken as a free parameter, and the minimum of  $\chi^2$

$$\chi^2(a_{nn}, F_N) = \sum_S \frac{\left( \frac{d^3\sigma_{a_{nn}}^{\text{MC}}(S)}{d\Omega_1 d\Omega_2 dS} - F_N \frac{d^3\sigma(S)}{d\Omega_1 d\Omega_2 dS} \right)^2}{\left( \Delta \frac{d^3\sigma(S)}{d\Omega_1 d\Omega_2 dS} \right)^2} \quad (29)$$

was calculated. As in Sec. VI, the  $\chi^2(a_{nn})$  values for a given  $nn$  FSI configuration were fitted with a quadratic polynomial to determine  $a_{nn}^{\text{shape}}$  and its statistical uncertainty  $\Delta a_{nn}^{\text{shape}}$  (see Fig. 20). To extract  $a_{nn}$ , we used only the three  $nn$  FSI configurations at  $\theta_{nn} = 20.5^\circ$ ,  $28.0^\circ$ , and  $35.5^\circ$ . The configuration at  $\theta_{nn} = 43^\circ$  had too few experimental cross-section points for a meaningful determination of  $a_{nn}$  from the shape of the cross section.

## VII. RESULTS FOR $a_{nn}$

Figures 21 through 24 show the experimental cross sections compared to MC generated finite-geometry  $nn$  FSI cross sections based on rigorous  $3N$  point-geometry calculations for  $a_{nn}$  values ranging from  $-17.0$  to  $-20.0$  fm. Here, the Bonn B  $NN$  potential model was used. Table I summarizes our results for the determination of  $a_{nn}$  from the absolute cross-section measurements. It presents the values for  $a_{nn}$  obtained using theoretical cross-section predictions of three realistic  $NN$  potential models. It is important to note that the  $a_{nn}$  values are practically independent of the  $NN$  interaction used.

The statistically averaged result for the neutron-neutron  $^1S_0$  scattering length obtained in this way is  $a_{nn} = -18.72 \pm 0.13$  fm. The associated uncertainty is the mean of the statistical error of the average  $a_{nn}$  obtained for each  $NN$  potential model using the squared statistical uncertainties as weighting factors. The systematic uncertainty taken as an average of the systematic uncertainties of all  $nn$  FSI configurations is  $\pm 0.65$  fm. Therefore, for  $a_{nn}$  determined from the absolute

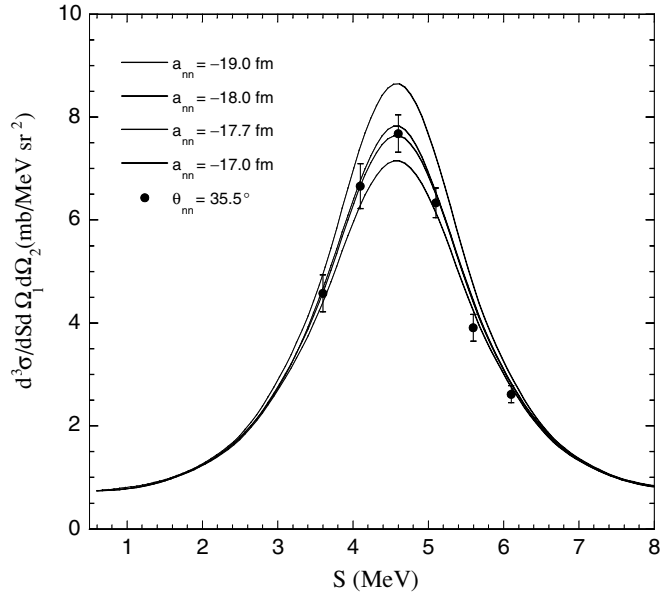


FIG. 23. Same as Fig. 21, but for  $\theta_{nn} = 35.5^\circ$ . Curves with the largest and smallest cross sections correspond to  $a_{nn} = -19.0$  fm and  $a_{nn} = -17.0$  fm, respectively.

$nn$  FSI cross-section data, we obtain

$$a_{nn} = -18.72 \pm 0.13 \pm 0.65 \text{ fm.} \quad (30)$$

The values obtained for  $a_{nn}$  from the shape analysis of the  $nn$  FSI cross sections are summarized in Table II. The weighted average is

$$a_{nn}^{\text{shape}} = -18.84 \pm 0.47 \text{ fm,} \quad (31)$$

with negligible systematic uncertainty.

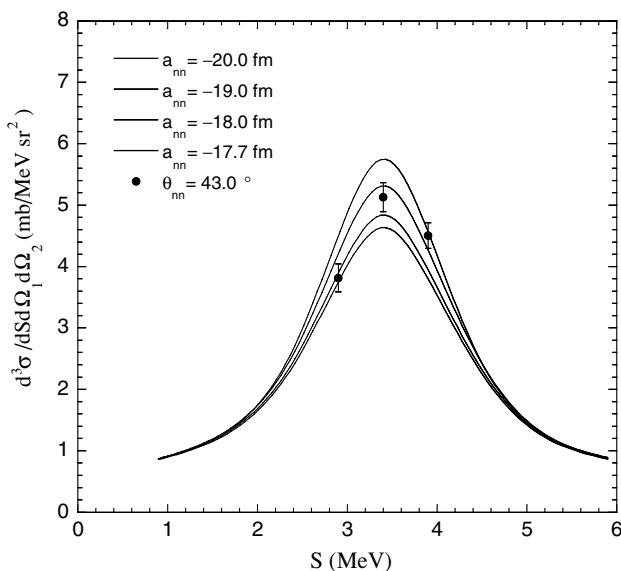


FIG. 24. Same as Fig. 21, but for  $\theta_{nn} = 43.0^\circ$ . Curves with the largest and smallest cross sections correspond to  $a_{nn} = -20.0$  fm and  $a_{nn} = -17.7$  fm, respectively.

TABLE I.  $a_{nn}$  values extracted from the absolute values of experimental cross sections for each particular  $nn$  FSI configuration by fitting cross sections generated by the Bonn B, CD Bonn, and Nijmegen I  $NN$  potentials.

$\theta_{nn}$	$a_{nn}$ (fm)	$\Delta a_{nn}^{\text{stat}}$ (fm)	$\Delta a_{nn}^{\text{syst}}$ (fm)
Bonn B			
20.5°	-18.9	$\pm 0.2$	$\pm 0.6$
28.0°	-18.8	$\pm 0.2$	$\pm 0.6$
35.5°	-17.7	$\pm 0.4$	$\pm 0.6$
43.0°	-18.8	$\pm 0.4$	$\pm 0.7$
CD Bonn			
20.5°	-18.9	$\pm 0.2$	$\pm 0.7$
28.0°	-18.6	$\pm 0.3$	$\pm 0.7$
35.5°	-17.8	$\pm 0.3$	$\pm 0.6$
43.0°	-18.6	$\pm 0.4$	$\pm 0.6$
CD Nijmegen I			
20.5°	-19.2	$\pm 0.2$	$\pm 0.8$
28.0°	-18.8	$\pm 0.3$	$\pm 0.7$
35.5°	-18.0	$\pm 0.3$	$\pm 0.6$
43.0°	-18.7	$\pm 0.4$	$\pm 0.6$

### VIII. COMPARISON WITH RECENT $a_{nn}$ DETERMINATIONS

Before we decided to perform this experiment, we tried to obtain detailed information about the previous most accurate kinematically complete  $nd$  breakup experiments. Our intention was to reanalyze these data with rigorous  $3N$  calculations, similar to what was done in Ref. [8] for kinematically incomplete  $nd$  breakup experiments. However, it turned out to be impossible to obtain important information about detector bias settings, electronic dead time, scatterer composition, finite geometry, etc. Therefore, we focus in the following only on the two most recent experiments.

The Erlangen group [39] determined the value of  $a_{nn} = -17.0 \pm 1.0$  fm from their kinematically complete  $nd$  breakup experiment at  $E_n = 13.0$  MeV and  $\theta_{nn} = 25^\circ$ . They used the W-matrix method [40] to analyze their absolute cross-section

TABLE II.  $a_{nn}$  extracted from the shapes of three  $nn$  FSI cross sections using Bonn B, CD Bonn, and Nijmegen I  $NN$  potentials.

$\theta_{nn}$	$a_{nn}$ (fm)	$\Delta a_{nn}$ (fm)
Bonn B		
20.5°	-19.0	$\pm 0.7$
28.0°	-18.3	$\pm 0.9$
35.5°	-18.8	$\pm 1.2$
CD Bonn		
20.5°	-19.1	$\pm 0.6$
28.0°	-18.3	$\pm 0.9$
35.5°	-18.8	$\pm 1.3$
CD Nijmegen I		
20.5°	-19.1	$\pm 0.6$
28.0°	-18.4	$\pm 0.9$
35.5°	-18.9	$\pm 1.3$

data. Were they to have used the rigorous calculations applied in the present work, they would have obtained  $a_{nn} = -14.4 \pm 0.3$  fm [18].

Because the Erlangen data are of high statistical accuracy, we performed a detailed shape analysis of their  $nn$  FSI cross-section data following the approach described in Sec. VI B. Rigorous point-geometry cross-section calculations were performed for  $\theta_{nn} = 25^\circ$  for  $-15$  fm  $< -a_{nn} < -20$  fm using the Bonn B  $NN$  potential model. MC-based finite-geometry calculations were not necessary because the Erlangen group, contrary to our approach, converted their experimental data, to point-geometry cross-section values. Because systematic deviations are apparent on the left wing of the cross-section curve (see Fig. 25), our shape analysis took into account only the cross-section data within the range  $4.1 \leq S \leq 8.1$  MeV. From the shape of the Erlangen cross-section data, we obtained, after renormalization by a factor of  $F_N = 1.41$ ,

$$a_{nn}^{\text{shape}} = -17.9 \pm 0.5 \text{ fm}. \quad (32)$$

This result is in reasonable agreement with the “expected” value for  $a_{nn}$ , suggesting that the Erlangen  $nn$  FSI cross-section data were incorrectly normalized.

Soon after the results of the present TUNL  $a_{nn}$  experiment were published in short form [26], the Bonn group [41], reported a result for  $a_{nn}$  which deviates considerably from our results. The Bonn experiment was performed at  $E_n = 25.3$  MeV and simultaneously at  $E_n = 16.6$  MeV. The  $nn$  FSI interaction was studied in “recoil geometry,” i.e., contrary to our approach (final-state geometry), only one of the two neutrons was detected but in coincidence with the associated proton, for which both energy and direction were measured. Using the same theoretical approach as employed in the present analysis, this kinematically complete experiment performed at one angle setting ( $\theta_{nn} = 55.5^\circ$  and  $\theta_{np} = 41.2^\circ$  on opposite sides of the incident neutron beam) resulted in a value of

$$a_{nn} = -16.3 \pm 0.4 \text{ fm}, \quad (33)$$

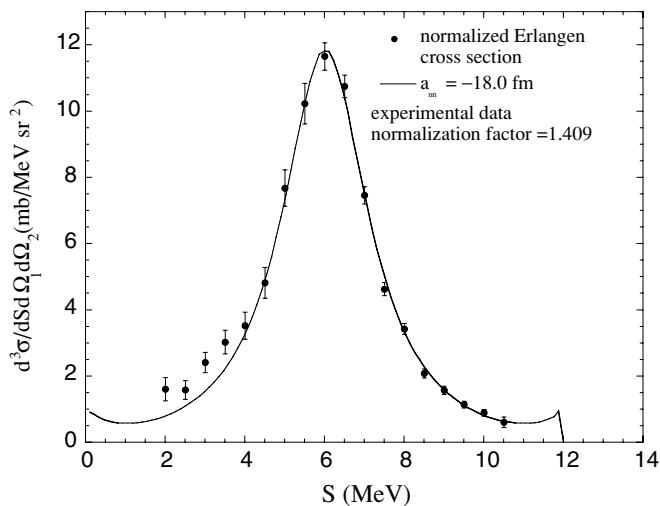


FIG. 25. Cross-section comparison for  $nn$  FSI configuration at  $\theta_{nn} = 25.0^\circ$  between the data of Ref. [39] normalized by 1.41 and 3N calculation using  $a_{nn} = -18.0$  fm. Incident neutron energy  $E_n = 13.0$  MeV.

as obtained from the absolute cross-section data at  $E_n = 25.3$  MeV, and

$$a_{nn} = -16.1 \pm 0.4 \text{ fm}, \quad (34)$$

when the data were normalized to the calculated neutron-proton quasi-free-scattering part of the measured spectrum. At  $E_n = 16.6$  MeV, only relative data were obtained, resulting in  $a_{nn} = -16.2 \pm 0.3$  fm. Clearly, these results are not only incompatible with our results and with the  $\pi^-d$  capture results for  $a_{nn}$ , but also with general arguments regarding the sign of CSB of the  $NN$  interaction. However, they agree with the pre-1990 average value for  $a_{nn}$  obtained from kinematically complete  $nd$  breakup experiments. Even more puzzling is the fact that the Bonn group obtained the correct result for  $a_{np}$  in separate  $nd$  breakup experiments at  $E_n = 25.2$  MeV in recoil geometry [41] and more recently also in final-state geometry [42].

## IX. SUMMARY AND CONCLUSION

The neutron-neutron  $^1S_0$  scattering length  $a_{nn}$  has been determined from a kinematically complete  $nd$  breakup experiment at  $E_n = 13.0$  MeV and four production angles of the  $nn$  pair between  $20.5^\circ$  and  $43.0^\circ$ . From the absolute FSI cross-section data, we obtained an angle averaged value of  $a_{nn} = -18.72 \pm 0.13 \pm 0.65$  fm, where the first uncertainty represents the statistical uncertainty and the second uncertainty is an estimate of the combined systematic uncertainties associated with the present analysis. We also performed a shape analysis of the FSI cross-section enhancement by allowing the data to float. In this case, we obtained the average value of  $a_{nn} = -18.84 \pm 0.47$  fm, which is in excellent agreement with the result obtained from the absolute cross-section data. For the first time, the present work provides precise results for  $a_{nn}$  obtained from kinematically complete  $nd$  breakup data which are in agreement with the expected value based both on  $\pi^-d$  capture data and on general theoretical arguments. Because our results do not exhibit a definite angular dependence for  $a_{nn}$  obtained at different production angles of the  $nn$  pair, 3NF effects on the  $nn$  FSI cross-section enhancements must be small. This finding is supported by the theoretical calculations shown in Fig. 26. Here, the percentage difference between the  $nn$  FSI cross section calculated with modern  $NN$  potential models plus the 3NFs TM99 and URIX and without these 3NFs is given at  $E_n = 13$  MeV as a function of the  $nn$  production angle.<sup>1</sup>

An important and unique cross-check of the present results has been the simultaneous determination of the neutron-proton scattering length  $a_{np}$  using the same neutron detectors that were used for the  $a_{nn}$  measurements. As will be described in detail in Part II [25], our results for  $a_{np}$  obtained from the  $nd$  breakup reaction at  $E_n = 13.0$  MeV are in very good agreement with the value known from free neutron-proton scattering.

<sup>1</sup>When the present experiment was planned and carried out, the theoretical predictions based on Bonn B and the TM 3NF predicted a zero crossing in the vicinity of  $43^\circ$  rather than the  $46^\circ$  angle given by the more recent theoretical calculations.

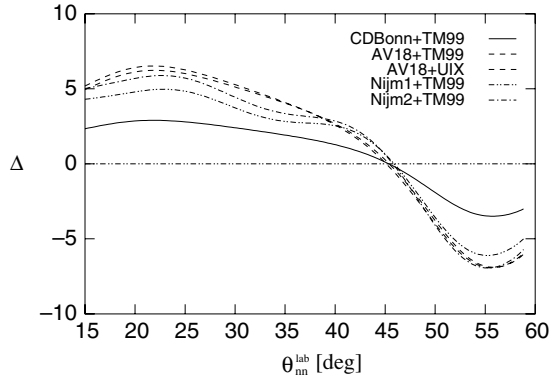


FIG. 26. Percentage deviation  $\Delta = [(\sigma(\text{NN} + 3\text{NF}) - \sigma(\text{NN}))/\sigma(\text{NN})] \times 100$  of the FSI cross section calculated with and without 3NFs as a function of the laboratory production angle of the  $nn$  pair.

Any deviation from the expected result for  $a_{np}$  would have resulted in a corresponding percentage change of our result for  $a_{nn}$ . It should be noted that the neutron detectors used for the  $a_{np}$  measurements and not directly used for the  $a_{nn}$  measurements were employed for determining the luminosity of the simultaneous  $a_{nn}$  and  $a_{np}$  measurements, making the  $a_{np}$  data an even more powerful cross-check on the correctness of the present results for  $a_{nn}$ . Common to the determination of  $a_{nn}$  and  $a_{np}$  are the efficiencies of the neutron detectors. As will be described in Ref. [43], a tremendous amount of work has been devoted to the accurate determination of the neutron detector efficiencies. The good agreement of our  $3N$  results for  $a_{np}$  with the two-body result and the excellent agreement obtained for  $a_{nn}$  from the absolute cross-section measurements and the shape analysis (with normalization

factors of close to 1.0) clearly proves that our neutron detector efficiencies are accurate. It would be hard to conceive a way that our results for  $a_{nn}$  are incorrect, considering the unique experimental correlations between the present  $a_{nn}$  and  $a_{np}$  determinations. On the other hand, we have no viable explanation why the result of the Bonn group for  $a_{nn}$  is different from our result, although their results for  $a_{np}$  agree with our result (and the two-body result). However, there is one important difference between the present data and the Bonn data. Our results for  $a_{nn}$  and  $a_{np}$  were obtained simultaneously in the same experiment and not in separate and to some extent independent experiments, as was the case for the Bonn data.

Presently, in collaboration with von Witsch of the Bonn group, an experiment is under development at TUNL at  $E_n = 19$  MeV with the goal of determining  $a_{nn}$  simultaneously in recoil geometry (using the Bonn group's detector hardware) and in final-state geometry (using the TUNL detector hardware). In addition,  $a_{np}$  will be measured simultaneously (in recoil geometry). It is expected that this ambitious project will resolve any issues regarding the value of  $a_{nn}$  obtained from kinematically complete  $nd$  breakup experiments performed in the two different FSI geometries.

#### ACKNOWLEDGMENTS

The numerical calculations were performed on the Cray T916 at the North Carolina Supercomputing Center in Research Triangle Park, NC, and on the Cray T90 and T3E at the John von Neumann Institute for Computing in Jülich, Germany. This work was supported in part by the U.S. Department of Energy, Office of Nuclear Physics, under Grant No. DE-FG02-97ER41033.

- 
- [1] W. Heisenberg, *Z. Phys.* **77**, 1 (1932).  
 [2] G. Miller, B. Nefkens, and I. Šlaus, *Phys. Rep.* **194**, 1 (1990).  
 [3] R. Machleidt, *Adv. Nucl. Phys.* **19**, 189 (1989).  
 [4] D. R. Tilley, H. R. Weller, and H. H. Hasan, *Nucl. Phys.* **A474**, 1 (1987).  
 [5] M. J. Moravcsik, *Phys. Rev.* **136**, B624 (1964); G. F. de Téramond, in *Proceedings of the Workshop on Spin and Symmetries, TRIUMF, Vancouver, June 30–July 2, 1989*, TRI-89-5, edited by W. D. Ramsey and W. T. H. van Oers (TRIUMF, Vancouver, 1989), p. 235.  
 [6] J. R. Bergervoet, P. C. van Campen, W. A. van der Sanden, and J. J. de Swart, *Phys. Rev. C* **38**, 15 (1988).  
 [7] R. B. Wiringa, V. G. J. Stoks, and R. Schiavilla, *Phys. Rev. C* **51**, 38 (1995).  
 [8] W. Tornow, H. Witała, and R. T. Braun, *Few-Body Syst.* **21**, 97 (1996).  
 [9] W. Breunlich, S. Tegesen, W. Bertl, and A. Chalupka, *Nucl. Phys.* **A221**, 269 (1974).  
 [10] B. Zeitnitz, R. Maschuw, and P. Suhr, *Nucl. Phys.* **A149**, 449 (1970); B. Zeitnitz, R. Maschuw, and P. Suhr, W. Ebenhöf, J. Bruinsma, and J. H. Stuivenberg, *ibid.* **A231**, 13 (1974).  
 [11] W. von Witsch, B. Gómez Moreno, W. Rosenstock, and K. Ettl, *Nucl. Phys.* **A329**, 141 (1979).  
 [12] Y. Onel, R. C. Brown, J. A. Edington, N. M. Stewart, and I. M. Blair, *Nucl. Phys.* **A304**, 51 (1978).  
 [13] B. Gabioud *et al.*, *Nucl. Phys.* **A420**, 496 (1984) and references therein.  
 [14] O. Schori, B. Gabioud, C. Joseph, J. P. Perroud, D. Rügger, M. T. Tran, P. Truöl, E. Winkelmann, and W. Dahme, *Phys. Rev. C* **35**, 2252 (1987).  
 [15] C. R. Howell *et al.*, *Phys. Lett.* **B444**, 252 (1998).  
 [16] I. Šlaus, Y. Akaishi, and H. Tanaka, *Phys. Rep.* **173**, 257 (1989).  
 [17] H. Witała, W. Glöckle, and T. Cornelius, *Phys. Rev. C* **39**, 384 (1988).  
 [18] W. Glöckle, H. Witała, D. Hüber, and J. Golak, *Phys. Rep.* **274**, 107 (1996).  
 [19] D. Hüber, H. Witała, and W. Glöckle, *Few-Body Syst.* **14**, 171 (1993).  
 [20] H. Witała, D. Hüber, W. Glöckle, W. Tornow, and D. E. Gonzalez Trotter, *Few-Body Syst.* **20**, 81 (1996); H. Witała, D. Hüber, W. Glöckle, J. Golak, A. Stadler, and J. Adam Jr., *Phys. Rev. C* **52**, 1254 (1995).

- [21] S. A. Coon, M. D. Scadron, P. C. McNamee, B. R. Barrett, D. W. E. Blatt, and B. H. J. McKellar, Nucl. Phys. **A317**, 242 (1979); S. A. Coon and W. Glöckle, Phys. Rev. C **23**, 1790 (1981).
- [22] S. A. Coon and J. A. Niskanen, Phys. Rev. C **53**, 1154 (1996).
- [23] S. A. Coon and H. K. Han, Few-Body Syst. **30**, 131 (2001).
- [24] B. S. Pudliner, V. R. Pandharipande, J. Carlson, S. C. Pieper, and R. B. Wiringa, Phys. Rev. C **56**, 1720 (1997).
- [25] F. Salinas Meneses *et al.*, to be submitted to Phys. Rev. C.
- [26] D. E. González Trotter *et al.*, Phys. Rev. Lett. **83**, 3788 (1999).
- [27] D. Hüber, H. Kamada, H. Witała, and W. Glöckle, Acta Phys. Pol. B **28**, 1677 (1997).
- [28] R. Machleidt, F. Sammarruca, and Y. Song, Phys. Rev. C **53**, R1483 (1996).
- [29] V. G. J. Stoks, R. A. M. Klomp, C. P. F. Terheggen, and J. J. de Swart, Phys. Rev. C **49**, 2950 (1994).
- [30] H. Witała, A. Nogga, D. Hüber, and H. Kamada, Phys. Lett. **B409**, 19 (1997).
- [31] W. Glöckle, *The Quantum Mechanical Few-Body Problem*, Vol. 273 of Lecture Notes in Physics (Springer-Verlag, Berlin, 1983), p. 3.
- [32] H. Witała, W. Glöckle, and H. Kamada, Phys. Rev. C **43**, 1619 (1991).
- [33] R. Machleidt, private communication.
- [34] V. G. J. Stoks, private communication.
- [35] E. Finckh, K. Geissdörfer, R. Lin, S. Schindler, and J. Strate, Nucl. Instrum. Methods Phys. Res. A **262**, 441 (1987).
- [36] H. Witała, W. Glöckle, and T. Cornelius, Nucl. Phys. **A491**, 157 (1989).
- [37] W. Tornow, W. Arnold, J. Herdtweck, and G. Mertens, Nucl. Instrum. Methods Phys. Res. A **244**, 477 (1986).
- [38] M. Drosg, Nucl. Sci. Eng. **67**, 190 (1978).
- [39] K. Gebhardt, W. Jäger, C. Jeitner, M. Vitz, E. Finckh, T. N. Frank, Th. Januschke, W. Sandhas, and H. Habertzettl, Nucl. Phys. **A561**, 232 (1993).
- [40] T. N. Frank, H. Habertzettl, T. Januschke, U. Kerwath, and W. Sandhas, Phys. Rev. C **38**, 1112 (1988).
- [41] V. Huhn, L. Wätzold, Ch. Weber, A. Siepe, W. von Witsch, H. Witała, and W. Glöckle, Phys. Rev. C **63**, 014003 (2000).
- [42] J. Deng, A. Siepe, and W. von Witsch, Phys. Rev. C **66**, 047001 (2002).
- [43] D. E. González Trotter *et al.*, to be submitted to Nucl. Instrum. Methods Phys. Res. A.